THERMODYNAMIC AND KINETIC STUDY

OF THE IRON-MANGANESE-SULFUR SYSTEM

AT 1300°C

By

HITOJI NAKAO, B.Sc.

A Thesis

Submitted to the Faculty of Graduate Studies

in Partial Fulfilment of the Requirements

for the Degree

Master of Engineering

McMaster University

September 1967

MASTER OF ENGINEERING   McMASTER UNIVERSITY
(Metallury)   Hamilton, Ontario.

TITLE: Thermodynamic and Kinetic Study of the Iron-Manganese-Sulfur

System at 1300°C.

AUTHOR: Hitoji Nakao, B.Sc. (Kyoto University)

SUPERVISOR: Professor J. S. Kirkaldy

NUMBER OF PAGES: ix, 85

SCOPE AND CONTENTS:

In this thesis, a thermodynamic and kinetic study of the iron-
manganese-sulfur system is described which is relevant to sulfide trans-
formations in commercial steel at soaking temperatures ($\sim 1300^{o}$C).
Equilibrium and diffusion couple experiments have been carried out to
explain the characteristics of formation of sulfides at 1300°C using
electron probe microanalysis and metallographic techniques. Apparent
semi-conductive behaviour of MnS, which can not be understood on the
basis of simple diffusion kinetics, was observed in the diffusion
experiments. The concept of the "virtual" diffusion path adequately
rationalized the reaction between Fe-Mn alloys and FeS. Information
about the constitution of the 1300°C ternary isotherm was obtained.

ACKNOWLEDGEMENTS

TABLE OF CONTENTS

LIST OF TABLES

LIST OF ILLUSTRATIONS

CHAPTER I

INTRODUCTION

Attention has been drawn to the iron-manganese-sulfur system at
1300°C by an earlier study of intermittent ferrite banding in butt-welded
steel pipes which leads to severe weld cracking(so-called "hook" cracks).[1]
This ferritic banding has been attributed to the local depletion of
manganese in the iron surroundings of sulfide inclusions due to the solid
state diffusion of manganese towards the sulfides during cooling of the
ingot or soaking process. Such an explanation would be viable if the
initial sulfide formed on solidification were FeS which subsequently
transformed to the more stable MnS during the cooling and subsequent
heat treatment. To understand this and other technological characteristics
of steel it is mandatory that a study of the thermodynamics and kinetics
of the iron-manganese-sulfur system be undertaken at soaking pit tem-
peratures(~1300°C). This study is part of a broader program concerning
the temperature range up to melting point of iron.[2]

Fundamental studies of this system at 1300°C have been to date
qualitative. Clark[3] has produced an approximate determination of the
equilibrium between the three phases, liquid FeS, solid MnS and γ-iron,
and obtained qualitative information about the kinetics of interaction
between liquid FeS and iron-manganese alloy.

In general then, the program undertakes to obtain quantitative
thermodynamic and kinetic information relevant to the iron-manganese-
sulfur system with a view to achieving a better understanding of sulfide

1

transformations at 1300°C. Equilibrium and kinetic studies of this system were therefore undertaken using the diffusion couple method and electron probe microanalysis.

CHAPTER II

REVIEW OF PREVIOUS WORK

This chapter summarizes previous work concerning diagrams in the
Fe-Mn-S system, the solubility of sulfur in iron-manganese alloys and
the available diffusion data.

2.1 Phase Diagrams for the Fe-Mn-S System

It is necessary to have a background knowledge of the phase
diagram of the Fe-Mn-S system for the understanding of kinetic behaviour.
Wentrup[4] discussed the Fe-Mn-S ternary phase diagram on the basis of
four binary phase diagrams and his summary is shown in Fig. 1. It is
important to examine carefully these binary phase diagrams with emphasis
on the vicinity of the temperature of 1300°C.

The Fe-Mn binary diagram in the iron-rich region is very simple
according to Hansen[5] and consists of a wide range of solid solution
for γ-iron. The manganese-rich side is liquid at 1300°C. There is a
very narrow γ+liquid phase field at approximately 60wt.% of manganese.

The Mn-S binary system has been investigated by Vogel and Hotop[6].
Of particular significance is the wide miscibility gap in the liquid state.
According to Schanaase[7] and Kroger[8] the stable green form of NaCl-
type MnS exists at 50at.% of sulfur. In the Fe-S system, the existence
of a eutectic reaction at 988°C is well known because of the phenomenon
of hot shortness in steels during hot rolling. Jensen[9] found the
liquidus to have a maximum at 1190°C at a non-stoichiometric composition

3
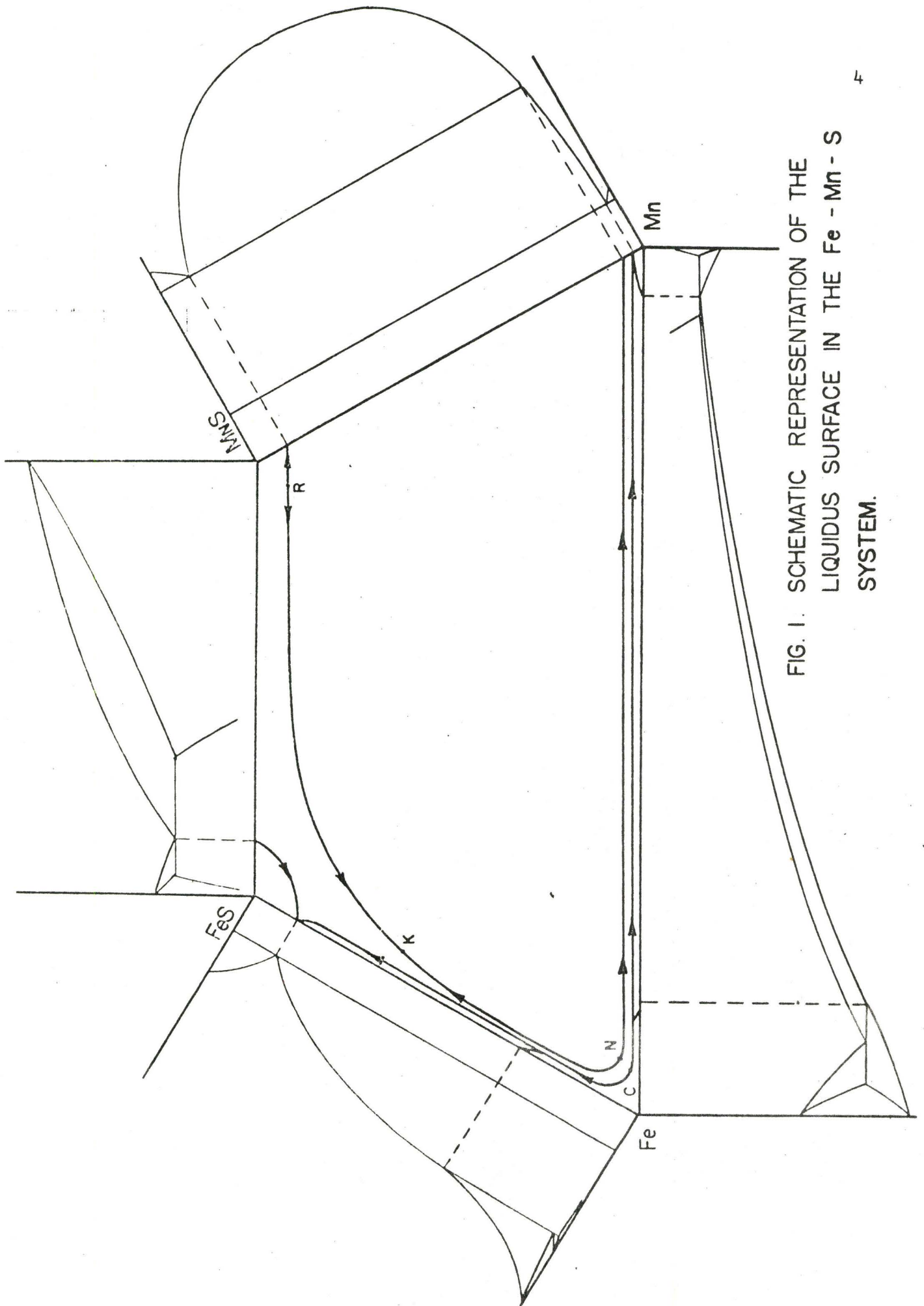
FIG. I. SCHEMATIC REPRESENTATION OF THE LIQUIDUS SURFACE IN THE Fe-Mn-S SYSTEM.

of FeS. The solid solubility of sulfur in Υ-iron is very low, a result which is very important to the understanding of the Fe-Mn-S system and it will be discussed further in the next section. Finally we have reported the existence of a pseudo-binary between FeS and MnS. This is supposed to be a simple eutectic with a large solid solubility of FeS in MnS[10]. Clark[3] has investigated this system at 1300°C, using an Fe-3.16%Mn vs. FeS diffusion couple, and has concluded that the supposed pseudo-binary system of FeS-MnS does not exist from the observation that the simple eutectic plane is curved towards a higher than stoichiometric sulfur content. His experiments are described more fully in 2.3.

2.2 Solid Solubility of Sulfur in Iron and Iron-Manganese Alloys

The iron-rich corner of the Fe-Mn-S system is the most important from the industrial point of view. The solid solubility of sulfur in iron in the temperature range 900to 1500°C has been determined by Rosenqvist and Dunicz[11] using measurements of the chemical activity of S in the solid solution by equilibration with a mixture of H_2 and H_2S. Turkdogan, Ignatowicz, and Pearson[12] have determined the solubility in iron at 1000°C, 1200°C, and 1335°C, and in iron-manganese alloys at 1200°C and 1350°C by a similar method. The results of both investigations in pure iron are in good agreement as shown in Fig.2. The solubility of sulfur in Υ-iron at 1300°C is 0.042wt.% from Fig.2. The sulfur solubilities in iron-manganese alloy at 1200°C and 1335°C after Turkdogan et al. are
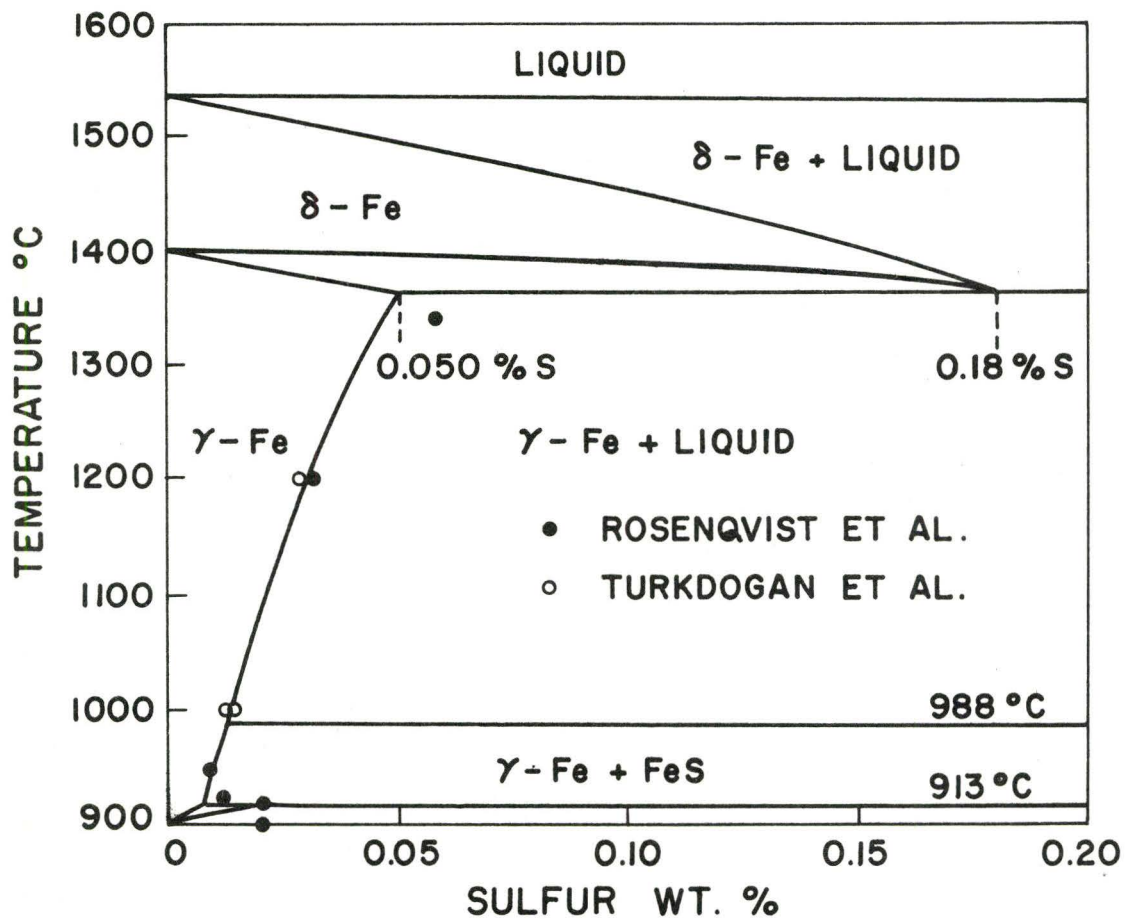
Fig. 2   Iron-rich corner of the Fe-S binary phase diagram after

Turkdogan et al.[12]

1200°C		1335°C	
Mn wt.%	S wt.%	Mn wt.%	S wt.%
0	0.031	0	0.046
0.037	0.0018	0.037	0.0058
1.07	0.00066	0.70	0.0032
1.30	0.00056	1.30	0.0018

It is seen that the presence of a small amount of manganese strongly reduces the solubility of sulfur in γ-iron. Turkdogan et al. also derived the solubility product of manganese and sulfur in γ-iron at various temperatures by the following method. The equilibrium constant of the reaction

$$(MnS) = [Mn] + [S] \qquad (2.1)$$

is

$$K = \frac{[\% Mn][\% S] f_S^{Mn}}{a_{MnS}} \qquad (2.2)$$

where f_S^{Mn} is the activity coefficient factor of sulfur in the presence of manganese. They find that

$$\log f_S^{Mn} = \left(-\frac{215}{T} + 0.097 \right) [\% Mn] \qquad \text{in γ-iron} \quad (2.3)$$

and the variation of the equilibrium constant K with temperature as

$$\log K = -\frac{9020}{T} + 2.29 . \qquad (2.4)$$

Brown[13] has recently proposed a sulfur potential diagram for the Fe-Mn-S system which purports to predict the solubility of sulfur in liquid and solid iron-manganese alloys by summarizing available thermochemical data for the Fe-Mn-S system.

2.3 The Study of the Fe-Mn-S System at 1300°C

Clark[3] investigated the Fe-Mn-S system at 1300°C by equilibrium and kinetic experiments. He used iron pots which contained manganese and iron sulfide for his equilibrium experiments, and designed diffusion couples between liquid FeS and solid Fe-3.16% Mn alloy in order to simulate manganese diffusion into FeS. The three-phase equibrium between γ-Fe, liquid FeS and solid MnS was observed by metallographic and electron probe microanalysis examination. Clark also observed the interface instability which develops between FeS and an Fe-Mn alloy and the manganese depletion near the interface due to solution in FeS. From these results Clark constructed the semi-schematic ternary isotherm in the Fe-Mn-S system at 1300°C, which is shown in Fig. 3. Clark recorded sulfur concentrations in both FeS and MnS phases equilibrated with γ-Fe which are much higher than the stoichiometric values which would apply to the supposed pseudo-binary between FeS and MnS at 1300°C and he suggested that the pseudo-binary might not exist at this temperature.

There is some doubt about the reliability of these experimental results. The iron pots and iron sulfide used were rather impure and contained a lot of oxygen. Oxide was usually observed between the

LIQUID FeS

STOICHIOMETRIC
FeS

β MnS

STOICHIOMETRIC
MnS

γ Fe

Fe

LIQUID Mn

Mn
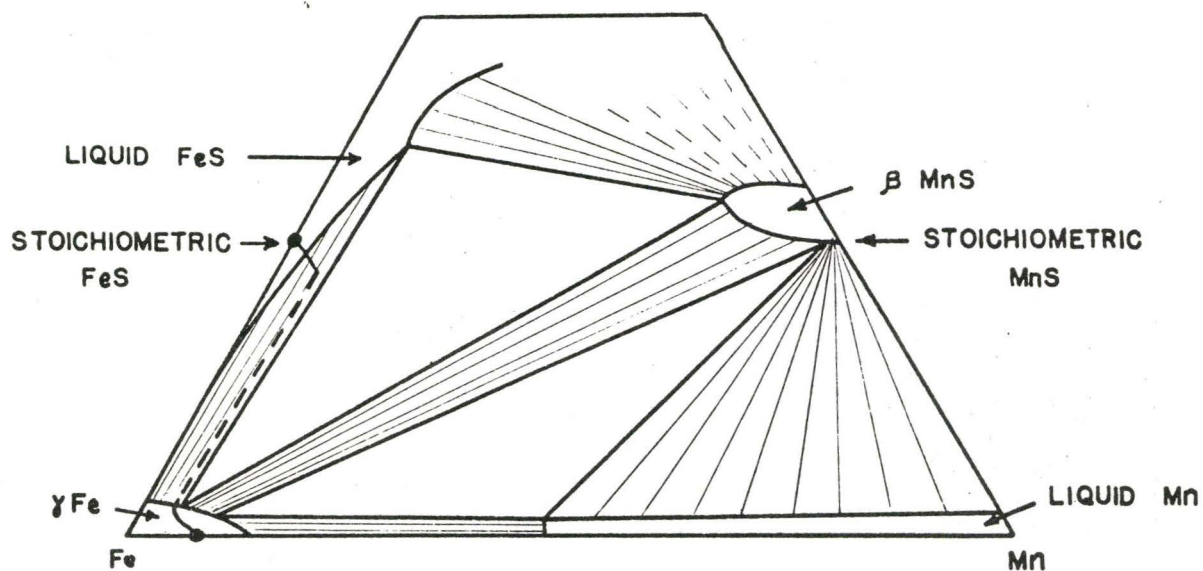
Fig. 3 Semi-schematic ternary isotherm in the system Fe-Mn-S
at 1300°C after Clark[3].

two sulfides. This means that oxygen might have shifted the equilibrium towards higher sulfur values. In the single high purity iron pot experiment, on which Clark placed most reliance, the iron sulfide was made by dropping levitated high purity iron into sulfur powder. The sulfur content of this iron sulfide could be far from the stoichiometric composition of FeS. Further, Clark's electron probe microanalysis was done on iron and manganese only, and the sulfur content was obtained by subtraction from 100%. The probe analysis could therefore cause appreciable error.

Although Clark's work represents a useful preliminary survey of the problem it is apparent that a more precise, quantitative investigation is required.

2.4 Diffusion Data

Diffusion data for manganese and sulfur in γ-iron at 1300°C is required for the kinetic study of this system. Following is a summary of published results. Wells and Mehl[14] report an empirical equation for the manganese coefficient in the range of manganese concentration 0 to 20% and temperature range 950 to 1450°C with the accuracy of 15%, viz.,

$$D = (0.486 + 0.011 \times wt.\%Mn) \exp(-\frac{66000}{RT}) \ . \tag{2.5}$$

Some experiments have been carried out in the present investigation to assess the validity of this result.

Bramley, Haywood, Cooper and Watts[15] measured the diffusion coefficient of sulfur between 1223°C and 1423°C, using rather impure

iron and obtained

$$D = 2.37 \times 10^{-6} \exp(-\frac{21300}{RT}) \quad cm^2/sec \; . \tag{2.6}$$

Ainslie and Seybolt[16] measured the diffusion coefficient of sulfur in 3.25% silicon-iron in the temperature range of 900 to 1300°C by radioactivity techniques and reported

$$D = 2.68 \exp(-\frac{49700}{RT}) \quad cm^2/sec \; . \tag{2.7}$$

Kononyuk[17] has measured the coefficient in high purity iron (spectral analysis revealed only traces of different metals, and carbon, phosphorus, sulfur, nitrogen were found by chemical analysis to be less than 0.003 to 0.004%), in the temperature range of 1150 to 1250°C. The temperature dependence of the sulfur diffusion coefficient in Υ-iron between 1150°C and 1250°C was described as:

$$D = 1.8 \times 10^{-2} \exp(-\frac{38600}{RT}) \quad cm^2/sec \; . \tag{2.8}$$

Equation (2.8) is assumed to be the most reliable and is used exclusively in the present study.

CHAPTER III

THEORY

In this chapter the kinetic theory pertinent to the iron-manganese-sulfur system will be discussed. The phenomenological theory of diffusion is the basis of the discussion so the ternary diffusion theory for single-phase and multi-phase systems will be presented. The concept of a "virtual" diffusion path will be found useful in the discussion of unstable interfaces which may be observed in multi-phase ternary diffusion couples.

3.1 Phenomenological Diffusion Theory

Irreversible phenomena are described by phenomenological equations of the general type given by Onsager[18],

$$J_i = \sum_{k=1}^{n} L_{ik} X_k \qquad (i = 1, 2, \cdots\cdots, n) \qquad (3.1)$$

where the X_k are forces, J_i are the fluxes caused by forces, and L_{ik} are phenomenological coefficients. Equation (3.1) states that any flux is caused by contributions of all forces. From this relation it may be inferred that in multicomponent diffusion the flux of each component is a linear function of all the independent concentration gradients. Fick's first law therefore becomes in one dimension for an n-component system,

12

$$J_i = - \sum_{k}^{n-1} D_{ik} \frac{\partial c_k}{\partial x} \qquad (i = 1, 2, \cdots, n-1) \qquad (3.2)$$

where the D_{ik} are diffusion coefficients, the c_k are concentrations in mass/unit volume and x is the distance.

By combining equation (3.2) with the corresponding mass balance,

$$\text{div } J_i + \frac{\partial c_i}{\partial t} = 0 \qquad (3.3)$$

one obtains the n-1 simultaneous diffusion equations in one dimension,

$$\frac{\partial c_i}{\partial t} = \sum_{k=1}^{n-1} \frac{\partial}{\partial x} \left[D_{ik} \frac{\partial c_k}{\partial x} \right]. \qquad (3.4)$$

These are the generalization of Fick's second law. Most problems involving the diffusion process will be reduced to solutions of the differential equations (3.4), by applying appropriate boundary conditions.

3.2 Binary Diffusion with a Constant Diffusion Coefficient

The binary diffusion equation with a constant diffusion coefficient in one dimension from equation (3.4) is

$$\frac{\partial c}{\partial t} = D \frac{\partial^2 c}{\partial x^2} . \qquad (3.5)$$

In a semi-infinite diffusion couple, the initial conditions are

$$
\left.\begin{array}{ll}
c = c_0 & \text{for } x > 0 \text{ and } t = 0 \\[2mm]
c = c_1 & \text{for } x < 0 \text{ and } t = 0
\end{array}\right\} \tag{3.6}
$$

and the corresponding solution to equation (3.5) after Barrer[19] is:

$$
c = c_0 + \frac{1}{2}(c_1 - c_0)\left(1 - \operatorname{erf}\frac{x}{2\sqrt{Dt}}\right). \tag{3.7}
$$

Differentiating equation (3.7), we obtain

$$
\left(\frac{\partial c}{\partial x}\right)\Big|_{x=0} = -\frac{1}{2}(c_1 - c_0)\frac{2}{\sqrt{\pi}}\frac{\partial}{\partial x}\int_0^{\frac{x}{2\sqrt{Dt}}} e^{-\xi^2}\, d\xi \tag{3.8}
$$

$$
= -\frac{1}{2}(c_1 - c_0)\frac{2}{\sqrt{\pi}}\frac{1}{2\sqrt{Dt}}.
$$

If the origin is chosen at the point which has the concentration $\frac{1}{2}(c_1 + c_0)$, then we have the alternative expression

$$
\frac{\partial c}{\partial x}\Big|_{x=0} = -\frac{1}{2z}(c_1 - c_0) \tag{3.9}
$$

where z is the intercept of the slope at the origin with the line c_0

lying parallel to x axis. Equating equations (3.8) and (3.9), one obtains the expression for the concentration independent diffusion co-efficient,

$$D = \frac{z^2}{\pi t} \qquad (3.10)$$

in terms of the empirical parameter z.

3.3 Ternary Diffusion in a Single-Phase System

The ternary diffusion equations in a single phase becomes in a one-dimensional system, assuming concentration independent diffusion coefficients,

$$\frac{\partial c_1}{\partial t} = D_{11} \frac{\partial^2 c_1}{\partial x^2} + D_{12} \frac{\partial^2 c_2}{\partial x^2} \qquad (3.11)$$

$$\frac{\partial c_2}{\partial t} = D_{21} \frac{\partial^2 c_1}{\partial x^2} + D_{22} \frac{\partial^2 c_2}{\partial x^2} \qquad (3.12)$$

where the off-diagonal diffusion coefficients D_{12} and D_{21} describe the diffusivity of one component on the concentration gradient of the other component. Parametric solutions of equations (3.11) and (3.12) were first obtained by Fujita and Gosting[20] in terms of the parameter

$$\lambda = \frac{x}{2\sqrt{t}} \qquad (3.13)$$

applicable to the following initial and boundary conditions for an infinite diffusion couple:

Initial conditions:

$$c_1 = c_{10}, \quad c_2 = c_{20} \quad \text{for} \quad x > 0, \quad t = 0$$
$$c_1 = c_{11}, \quad c_2 = c_{21} \quad \text{for} \quad x > 0, \quad t = 0$$

(3.14)

Boundary conditions:

$$c_1 = c_{10}, \quad c_2 = c_{20} \quad \text{for} \quad x \to +\infty, \quad t = t$$
$$c_1 = c_{11}, \quad c_2 = c_{21} \quad \text{for} \quad x \to -\infty, \quad t = t$$

(3.15)

The solutions are

$$c_1 = c_{11} + a \text{ erf } (\sqrt{p} \, \lambda) + b \text{ erf } (\sqrt{q} \, \lambda)$$

(3.16)

$$c_2 = c_{21} + d \text{ erf } (\sqrt{p} \, \lambda) + e \text{ erf } (\sqrt{q} \, \lambda)$$

(3.17)

where a, b, d, and e depend on the boundary concentrations and the diffusion coefficients and where p and q depend on the diffusion coefficients.

The off-diagonal diffusion coefficients, D_{12} and D_{21} can be estimated in terms of thermodynamic interaction coefficients. Kirkaldy and Purdy[21] have derived the expressions applicable to dilute ternary solutions,

$$\frac{D_{12}}{D_{11}} \simeq \epsilon_{12} N_1$$

(3.18)

$$\frac{D_{21}}{D_{22}} \simeq \varepsilon_{12} N_2 \tag{3.19}$$

where ε_{12} is the interaction parameter defined by,

$$\varepsilon_{12} = \frac{\partial (\ln f_1)}{\partial N_2} \quad , \tag{3.20}$$

where f_1 is the activity coefficient of component one and N_2 is molar fraction of component two. These approximations are valid for the iron-rich portion of the Fe-Mn-S ternary system. Equations (3.16) and (3.17) may be simplified when the following conditions are satisfied,

$$(D_{22} - D_{11})^2 \gg 4 D_{12} D_{21}$$

$$\tag{3.21}$$

$$\text{and} \qquad D_{11} D_{22} \ggg D_{12} D_{21} \quad .$$

(3.16) and (3.17) then become

$$c_1 = c_{11} + \left\{ (c_{10} - c_{11}) - \frac{D_{12}}{D_{22} - D_{11}} (c_{20} - c_{21}) \right\} \text{ erf } \left(\frac{x}{2\sqrt{D_{11}t}}\right)$$

$$+ \frac{D_{12}}{D_{22} - D_{11}} (c_{20} - c_{21}) \text{ erf } \left(\frac{x}{2\sqrt{D_{22}t}}\right) \tag{3.22}$$

$$c_2 = c_{21} - \frac{D_{21}}{D_{22} - D_{11}} (c_{10} - c_{11}) \, \text{erf} \left(\frac{x}{2\sqrt{D_{11}t}} \right)$$

$$+ \left\{ (c_{20} - c_{21}) + \frac{D_{21}}{D_{22} - D_{11}} (c_{10} - c_{11}) \right\} \text{erf} \left(\frac{x}{2\sqrt{D_{22}t}} \right) \qquad (3.23)$$

which will tend, in view of (3.18) and (3.19), to become valid as the solutions become increasingly dilute. If the ternary solution is extremely dilute, for example, within the solubility limit of manganese and sulfur in Υ-iron at 1300°C, the off-diagonal diffusion coefficients become so small compared to the on-diagonal coefficients that equations (3.22) and (3.23) can be further simplified to the binary relations,

$$c_1 = c_{11} + (c_{10} - c_{11}) \, \text{erf} \left(\frac{x}{2\sqrt{D_{11}t}} \right) \qquad (3.24)$$

and

$$c_2 = c_{21} + (c_{20} - c_{21}) \, \text{erf} \left(\frac{x}{2\sqrt{D_{22}t}} \right) \qquad (3.25)$$

It has been suggested that the diffusion path can be mapped onto the ternary isothermal phase diagram by Darken[22] and by Rhines, Meussner and DeHoff[23]. Kirkaldy and Brown[24] have systematized this procedure by stating a number of theorems for the representation of diffusion paths for single-phase infinite diffusion couples on an isothermal section of the ternary constitution diagram. These diffusion paths are defined uniquely by the terminal compositions and according to

Meijering[25] must cross the straight line joining the terminal composi-
tions at least once.

3.4 Ternary Diffusion in Multi-Phase Systems

The two independent concentration gradients in a ternary multi-
phase system lead to the possibility of unstable phase interfaces.
Such unstable interfaces were observed matallographically and qualita-
tively in the Al-Mg-Zn ternary system by Clark and Rhines[26]. Similar
unstable oxide phase interfaces have been observed in the oxidation of
binary alloys. For the theoretical discussion of instability in the
Fe-Mn-S ternary system we will invoke the concept of the virtual diffusion
path developed by Kirkaldy and Fedak[27], and by Kirkaldy and Brown[24].

3.4.1 The Virtual Diffusion Path on a Ternary Isotherm

The phase rule indicates that an extra degree of freedom exists
at a phase boundary for a ternary system under isothermal and isobaric
conditions. Indeed, infinite ternary diffusion couples terminating in
different phases often lead to supersaturation which produces precipi-
tates or non-planar interfaces. The calculation of such unstable
diffusion paths seems to be impossible of exact solution. Kirkaldy and
Brown[24] have therefore suggested the following procedure. One first
obtains a complete parabolic (λ-dependent) solution by matching solutions
of equations (3.16) and (3.17) at phase interfaces on the assumption
that they are planar. This is called a "virtual" path. The "virtual"
path can be calculated from diffusion equations (3.16) and (3.17), first
by assuming that the interfaces are planar, and secondly by guessing the

order of phases appearing between the terminal compositions. If the
solution obtained does not lead to supersaturation the solute distri-
bution is non-virtual and the diffusion path is an actual one which
always coincides with tie-lines in two-phase regions. If the calculated
path crosses tie-lines in two-phase regions the diffusion path must be
regarded as a "virtual" path.

A schematic "virtual" diffusion path on a ternary isotherm leading
to both isolated and non-isolated regions of supersaturation is shown in
Fig. 4 after Kirkaldy and Brown. Wherever the path crosses tie-lines we
may expect instability or precipitation. This thermodynamic characteristic
is quite analogous to constitutional supercooling which can occur during
alloy solidification as shown in Fig. 5.

At the A end of the diffusion couple of Fig. 4 the diffusion
path passes into the two-phase region from the single-phase one at an
angle to the tie-lines and returns immediately to that same single phase.
This indicates that a region of isolated precipitates may form. At the
B end of the diffusion path, the region of supersaturation is in contact
with the tie-line, so both isolated precipitates and a non-planar mor-
phology become possible.

The "virtual" diffusion path could conceivably be the real path
in the absence of nucleation sites. This is unlikely to be the case in
a solid.
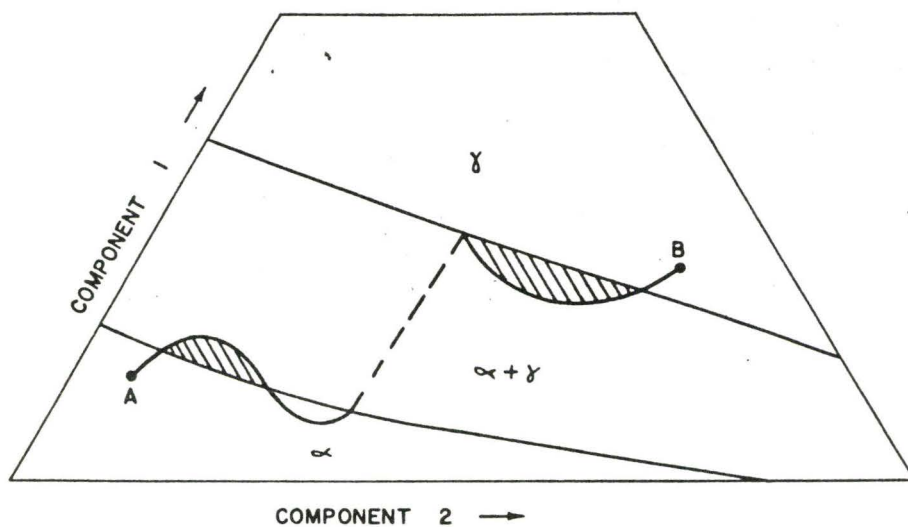
Fig. 4 Schematic diffusion path on a ternary isotherm showing isolated
and non-isolated supersaturation after Kirkaldy and Brown[24].
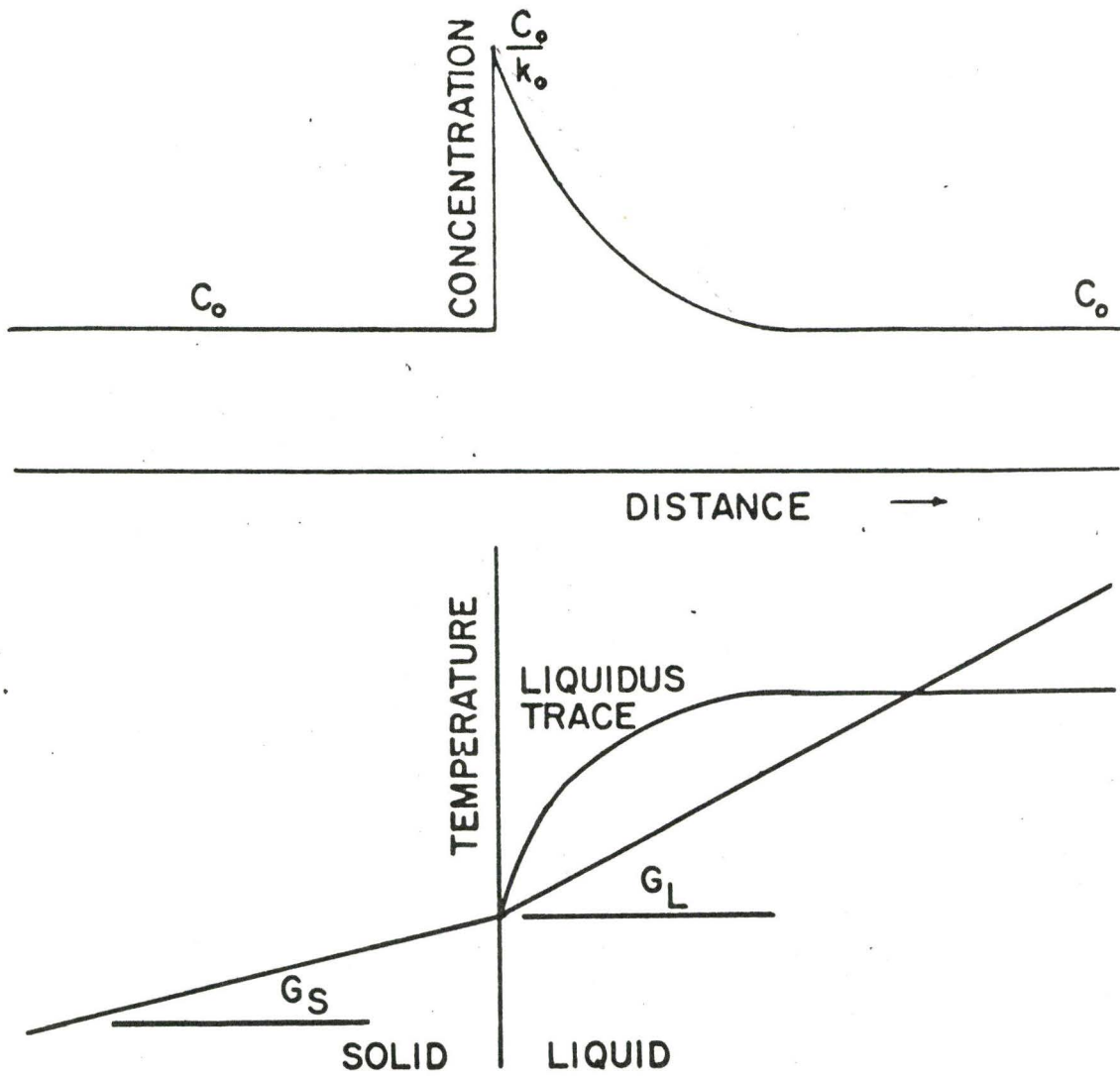
Fig. 5   Actual and constitutional temperature profiles in relation
to the concentration distribution during alloy solidification.

CHAPTER IV

EXPERIMENTAL METHOD

This chapter is concerned with the preparation of sulfides and
of the iron-manganese alloys, the construction of the diffusion couples,
the diffusion annealing apparatus and the electron probe microanalysis.

Altogether four types of experiments were carried out for the
equilibrium and kinetic studies in this system.

i)   Equilibrium experiments involving γ-iron, iron sulfide (FeS) and
     manganese sulfide (MnS)

ii) Measurement of the manganese diffusion coefficient in γ-iron

iii) Kinetic experiment using diffusion couples between iron sulfide
     and manganese sulfide

iv) Kinetic experiments using diffusion couples between iron, iron-
     manganese alloys and manganese sulfide

All specimens were examined metallographically and analysed by
electron probe microanalysis following equilibration or diffusion anneal-
ing.

4.1 Preparation of Materials

4.1.1 Iron and Iron-Manganese Alloys

Vacuum melted iron, Ferrovac E, was used for the measurement
of the manganese diffusion coefficient in γ-iron.

For the equilibrium and kinetic studies with sulfides, purer
oxygen-free iron was necessary to avoid the effect of oxygen on the

morphology of the sulfides as described in Clark's work in Chapter II.
For these purposes, zone-refined Battelle Memorial Institute's Iron was
supplied by the American Iron and Steel Institute. Electrolytic manga-
nese was used in the production of the alloys. The analysis of the
starting materials is given in Table I.

Table I

Analysis of Base Material

(in p.p.m by weight)

	C	Si	Mn	P	S	Cu	Ni	Cr	V	Mo	Co	H	O	N
Ferrovac E	30	<60	10	30	50	< 10	<140	<100	<40	<10	100	5	7.8	2
Battelle Iron	8	<2	1	3	0.6	2	6	10		0.2	0.8	7	0.06	1.5	<0.2

	Mg	Si	Fe	
Electrolytic Manganese	20	3	2	Mn = 99.99 weight per cent

Portions of each material were weighed to yield alloys containing
up to 10 weight per cent manganese. Approximately 35 to 45 grams of
material was placed into the melting chamber of a non-consumable arc
furnace. A tungsten electrode was used for the melting operation, which
was carried out under an atmosphere of 200 mmHg of argon. In order to
prevent oxidation by the argon during melting, a titanium oxygen getter
was used. Each charge was melted, inverted, and then remelted, until
a total of four melting operations had been completed, in order to pre-
vent long range segregation. The product was a button approximately 25
mm in diameter and 7 mm thickness for the manganese diffusion coefficient

measurements and a rod approximately 11 mm in diameter and 60 mm in length for the diffusion couples of the kinetics experiments. The buttons were cold rolled to a thickness of approximately 1.2 mm. The rods were swaged to a diameter of 9 mm. Cold rolled sheets and swaged rods were annealed for homogenization in a vacuum of 10^{-5} mmHg at 1300°C for 10 days. The chemical analysis for the manganese content of the sheets and rods is given in Table II.

Table II

Manganese-Weight Per Cent in Iron

Sheet	1.27	2.43	4.2	6.14
Rod	0.80	1.08	4.52	9.30

4.1.2 Iron Sulfide and Manganese Sulfide

As commercially available, iron sulfide (FeS) and manganese sulfide (MnS) contain far too much oxygen. These sulfides were therefore produced synthetically by sintering from iron, manganese and sulfur powder, as suggested by Kiessling and Westman[28], Furuseth and Kjekshus[29], and Argyriades, Derge and Pound[30]. Electrolytic iron powder (99.95%), electrolytic manganese (99.9%) and spectrographically pure sulfur (99.999%) were used as base materials. These materials were sorted to a powder of -80 mesh, and accurately weighed to yield FeS and MnS of stoichiometric composition. Each mixture of FeS and MnS was compressed to a cylinder of 8 mm in diameter and 10 to 25 mm in length, and sealed in an evacuated quartz tube at 10^{-5} mmHg. They were then heated very slowly up to 1000°C for FeS and 1150°C for MnS. The total heating time was approximately

200 hrs. After establishing equilibrium the samples were quenched in ice water. MnS powder crushed from the above samples was examined by the X-ray Debye-Sherrer powder method and identified as the NaCl type of structure from ASTM X-Ray Data File[31]. The observed lattice parameter is 5.22 Å which is to be compared with the value 5.224 Å given in the ASTM File.

The FeS and MnS were melted and solidified in an evacuated quartz tube and a graphite crucible in an argon atmosphere, respectively. Both sulfides showed no secondary phases by metallographic observation.

The sulfides were chemically analyzed with the following results.

$$Mn \text{ in } MnS = 62.4 \pm 1.0\%$$
$$Fe \text{ in } FeS = 63.1 \pm 0.5\%$$

Both are seen to be very close to the stoichiometric values.

4.2 Experimental Apparatus and Procedure

4.2.1 Preparation of Specimens

Four types of specimens were prepared for the experiments on iron-FeS-MnS equilibrium, iron vs. iron-manganese diffusion couples, iron-manganese vs. MnS diffusion couples and Fes-MnS diffusion couples.

i) Iron-FeS-MnS equilibrium specimen

Battelle iron sheet of 2 mm in thickness was cut into plates 1 cm x 1.2 cm, and melted and solidified MnS was polished into platelets of 2 mm in thickness. The MnS specimen was sandwiched between two layers of an iron sheet. These layers were welded in a hydrogen flow for 60 min. at 800°C. The resulting specimen was placed in a quartz tube with

sintered FeS and evacuated to 6×10^{-6} mmHg. The quartz tube was then located vertically in the center of the diffusion annealing furnace (see below) annealed for 60 min. at 1300°C, then quenched into ice water thus breaking the quartz tube.

ii) Iron-Manganese Binary Diffusion Couples

Iron and iron-manganese sheets of 1.2 mm in thickness were cut into plates of 8 mm x 10 mm and polished to 1 μ diamond, chemically cleaned, then clamped and welded in a hydrogen flow for 60 min. at 600°C. These diffusion couples were diffusion annealed in the vertical furnace for 54 hrs. at 1150°C, 27 hrs. at 1225°C, 5.5 hrs. at 1300°C and 4 hrs. at 1350°C, respectively, then quenched into ice water.

iii) Iron-Manganese Alloy vs. MnS Diffusion Couples

Pure iron vs. MnS diffusion couples of sandwich type were prepared as mentioned in i). Although the preparation of the iron-manganese vs. MnS diffusion couples was attempted in the same way, they did not adequately weld. Hence, another method was introduced to prepare these couples. The apparatus is shown photographically in Fig. 6, and schematically in Fig. 7. A 9 mm ϕ rod of iron-manganese alloy was suspended vertically inside of a 20 mm ϕ pyrex tube in which hydrogen was flowing. The bottom of the iron-manganese alloy rod was inductively heated by a copper coil of 3.2 mm in diameter, which was connected to a 10 KW, 450 KC/S Tocco generator, and the end was melted into a droplet of approximately 7 mm in diameter. The fused iron-manganese droplet fell into the water-cooled copper mold in which MnS was located and completely surrounded the MnS. As the cooling was almost instantaneous it is assumed that diffusion between iron-manganese alloy and MnS was negligible
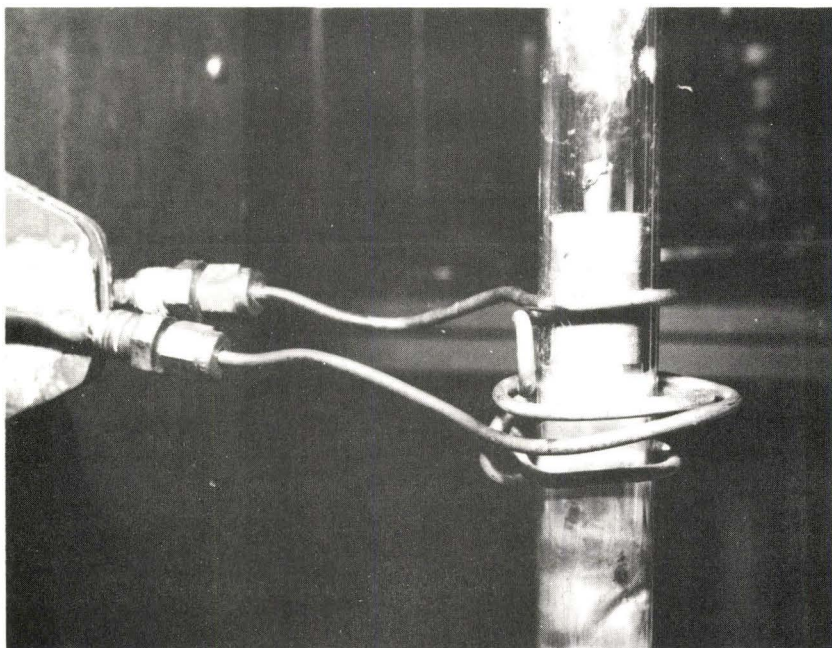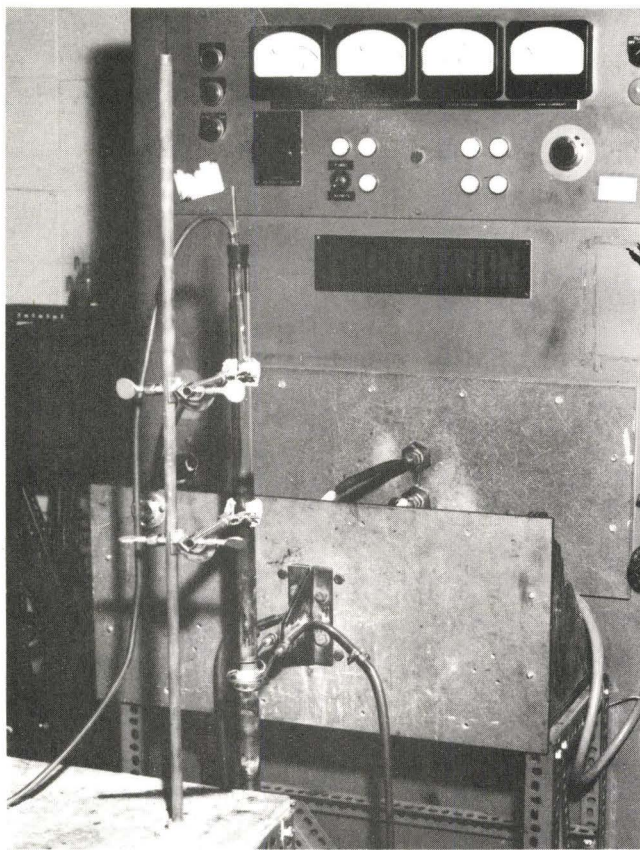
Fig. 6   Photograph of the apparatus for making Fe-Mn alloy vs. MnS
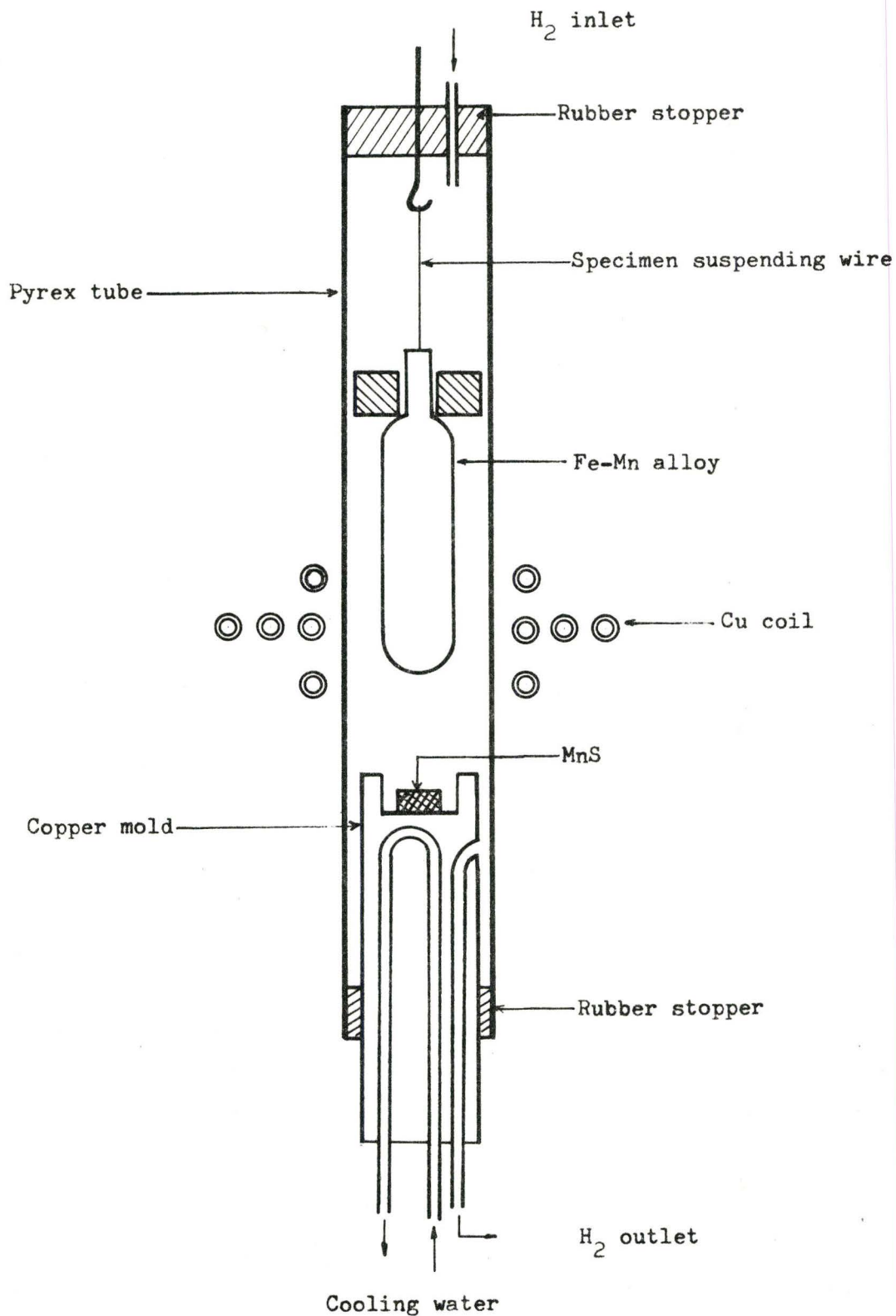
diffusion couples.

Fig. 7   Schematic cross section of the apparatus for making Fe-Mn alloy vs. MnS diffusion couples.

compared with that which occurred during the later diffusion anneal. These diffusion couples were then diffusion annealed in an argon atmosphere or in vacuum for 4 to 36 hrs. at $1300^{\circ}C$, then quenched into ice water.

iv) FeS vs. MnS diffusion Couples

Sintered FeS and solidified MnS were placed in a quartz tube, and evacuated to 7×10^{-6} mmHg. The quartz tubes were suspended in the vertical furnace at a temperature of $1300^{\circ}C$. The FeS melted instantly and diffusion took place between FeS and MnS. After from 6 min. to 60 min., the diffusion couples were quenched into ice water by dropping the quartz tubes.

4.2.2 Diffusion Annealing Apparatus

The apparatus used for diffusion annealing is shown photographically in Fig. 8, and schematically in Fig. 9.

The apparatus consisted of argon gas purification train and a vertical furnace. As MnS was very easy to oxidize at high temperature, the purification of argon gas had to carried out very carefully. High purity argon ($>99.999\%$) supplied by the Matheson Co. was used and an analysis is given in Table III.

Table III

Analysis of High Purity Argon

(p.p.m)

O_2	N_2	CH_4	CO	CO_2	H_2	H_2O
5.0	5.0	2.0	1.0	1.0	1.0	1.8
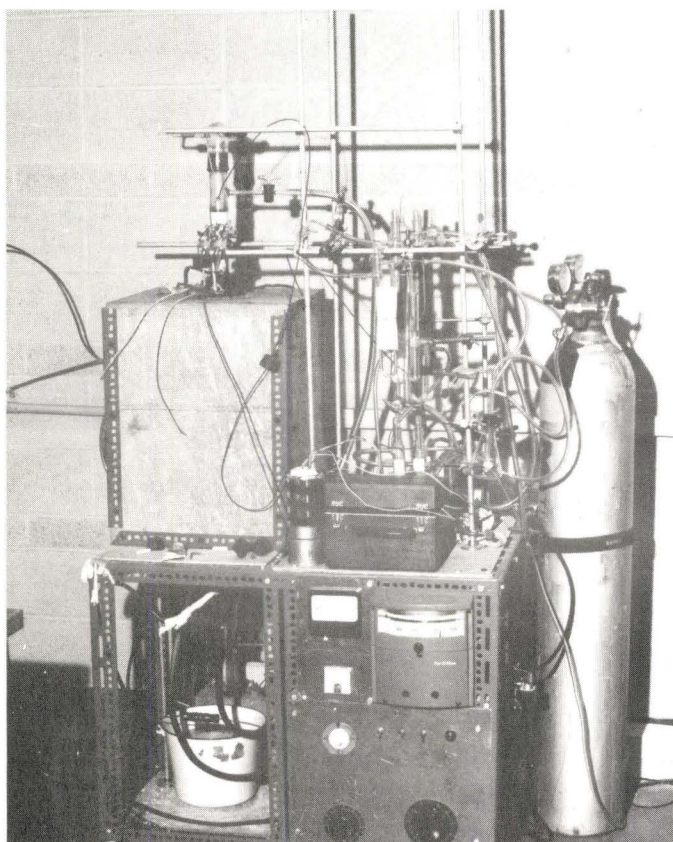
Fig. 8   Photograph of the diffusion annealing apparatus.
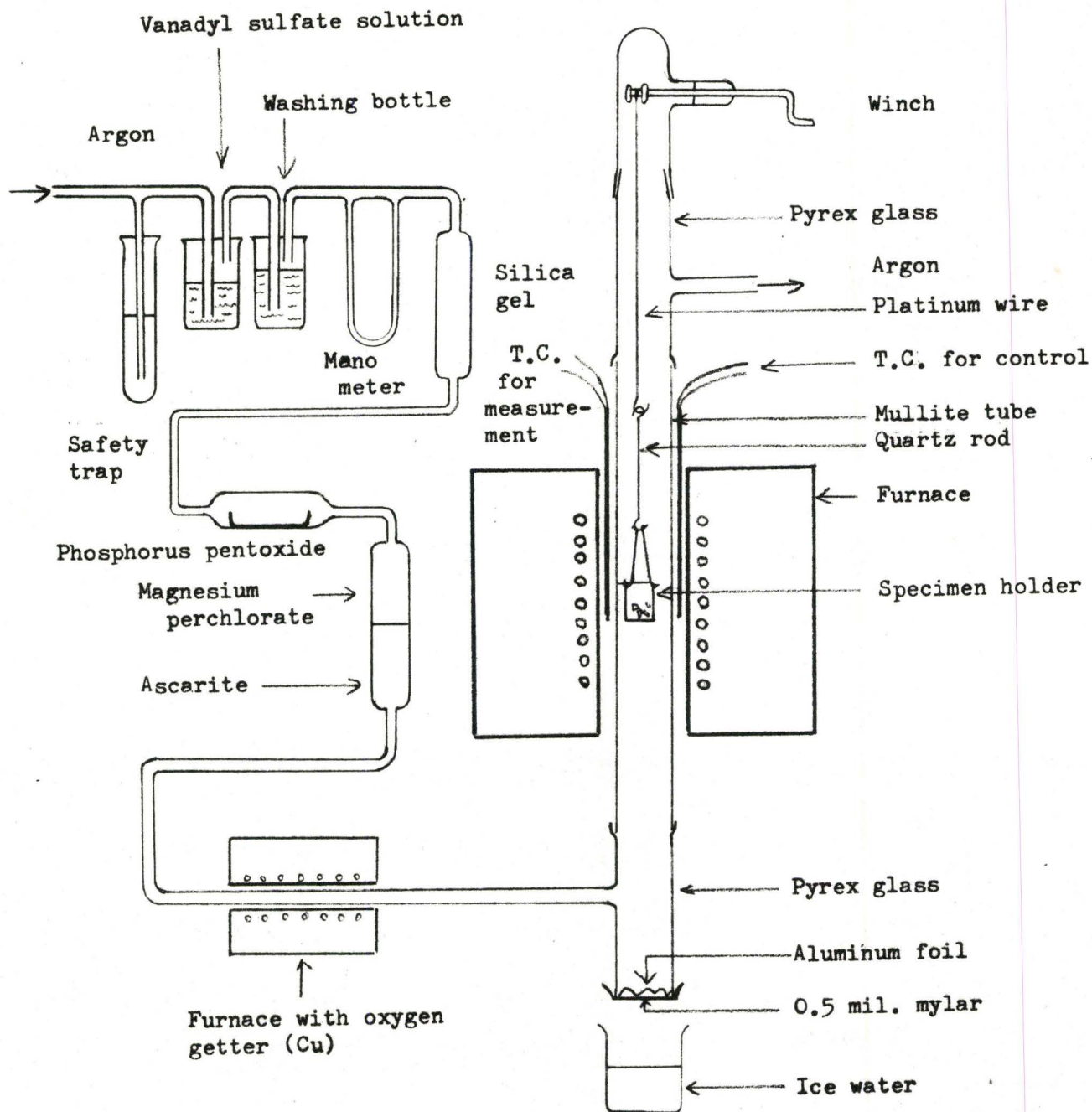
Fig. 9 Schematic cross section of the diffusion annealing apparatus.

The argon was passed through a vessel containing 0.1 M vanadyl sulfate solution together with lightly amalgamated 20 to 30 mesh zinc powder, in order to remove oxygen, and another vessel containing water to ensure removal of vanadium from the emergent gas stream, as described by Meites and Meites[32]. Water vapor was removed by absorption in drying reagents, such as silica gel, phosphorus pentoxide and magnesium perchlorate. Carbon dioxide was removed with Ascarite. The argon was further purified by allowing the gas to flow over a mixture of copper turnings and titanium shot maintained at a temperature of $600^{o}C$ in a small resistance furnace.

The furnace assembly consisted of a Kanthal A-1 wound heating element of 71 mm inside diameter and 51 cm length embedded in insulation materials. Inside the heating elements a 39 mm diameter mullite tube was located, which was directly sealed to the pyrex tubing. Power was supplied to the element by means of a 2500 VA transformer. The temperature was controlled to $\pm 2^{o}C$ by a Honeywell temperature controller and a Pt-10% Rh-Pt thermocouple. The control thermocouple was located between the Kanthal windings and the mullite tube, and a measuring Pt-13% Rh-Pt thermocouple was placed in the same position at the same level. The temperature inside the mullite tube at the specimen location was measured regularly with another measuring thermocouple. It was found that the temperature at the specimen location was lower by $18\pm1^{o}C$ than that of the measuring thermocouple throughout the course of the experiments and this was corrected for in the temperature record. The hot zone was 5 cm long with a temperature variation of $3^{o}C$. In view of possible calibration and recording errors we are quoting our experimental

temperatures to $\pm 5^{\circ}$C.

The bottom of the pyrex glass was sealed with a 0.5 M Mylar film on which aluminum foil was placed in order to prevent radiation of heat.

A schematic cross-section of the specimen holder assembly is shown in Fig. 9. A quartz bucket of 18 mm diameter and 40 mm in height with some holes of 1 mm diameter in the lower half portion, was suspended from a glass winch by a 0.13 mm diameter platinum wire and 2 mm diameter quartz rods. The diffusion couple was placed in the upper portion of the bucket and titanium was placed in the bottom as an oxygen getter. As some diffusion couples were sealed in quartz tubes, the quartz tubes were connected to the quartz rod by fusing.

When the temperature of the furnace reached the equilibrium point, the specimen was lowered into the hot zone by rotating the glass winch. After diffusion annealing the specimen was quenched into ice water by winching the platinum wire off and breaking the 0.5 M Mylar film.

Quenched specimens were mounted in bakelite and metallographically polished. The final surface was prepared by polishing on Buehler micro-cloth impregnated with 1 micron diamond grit and lubricated with kerosene. Each specimen was examined metallographically and analyzed by electron probe microanalysis.

4.3 Electron Probe Microanalysis

4.3.1 The Electron Probe Microanalyser

The electron probe microanalyser is an instrument for X-ray spectrochemical analysis of the surface of a solid specimen. It consists
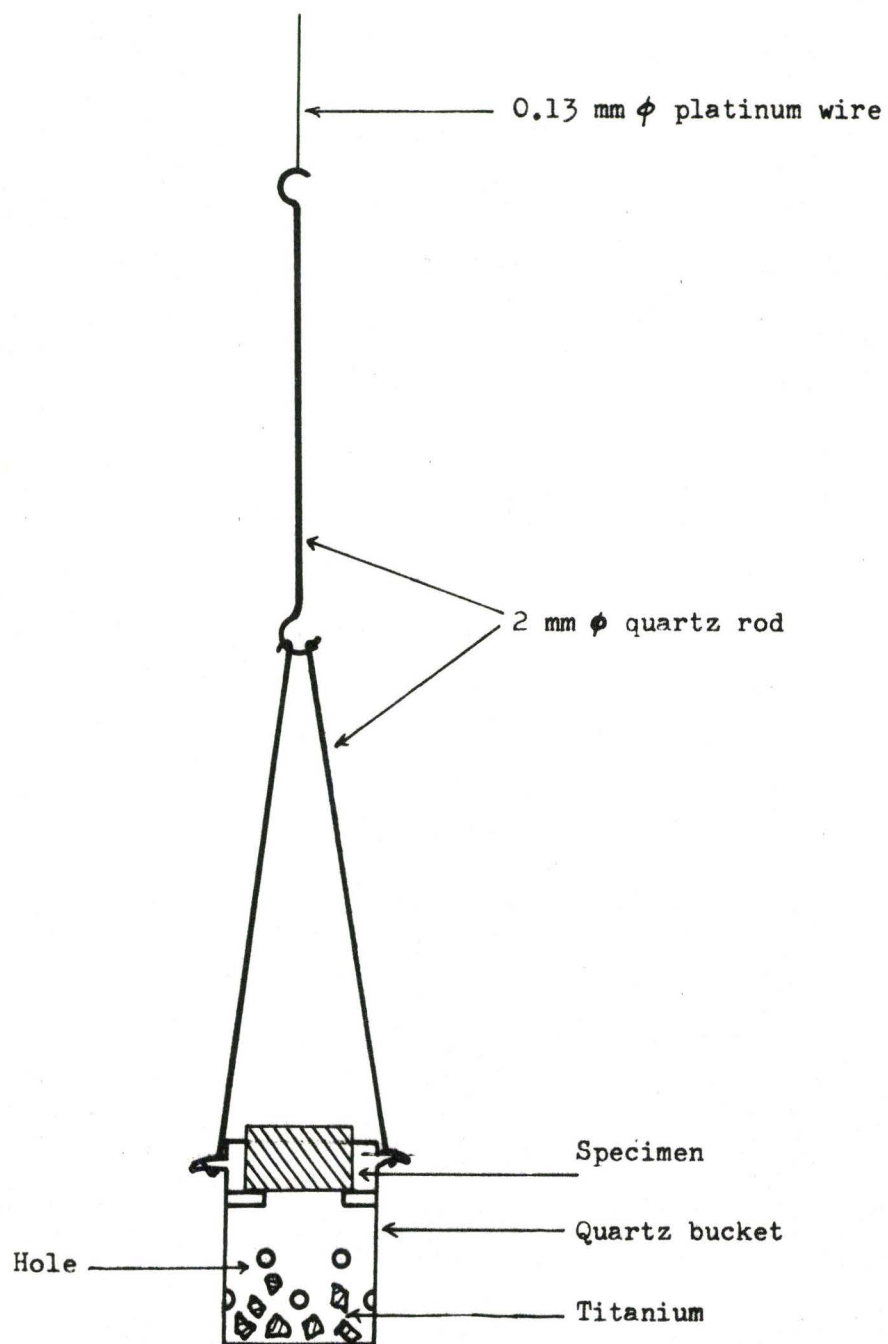
Fig. 10   Schematic cross-section of the specimen holder.

of three basic components, electron optics, X-ray optics and viewing
system. In the electron optics system, a beam of electrons accelerated
to 10 to 50 KV is focussed to a diameter of 0.1 to 3 μ on the specimen.
Where the electrons strike the specimen they generate the characteristic
X-ray spectra of the chemical elements contained in the area irradiated
to a depth of about 1 to 3 μ below the surface. The emitted X-rays are
analysed both qualitatively and quantitatively in an X-ray optical sys-
tem according to wave length and intensity. The specimen viewing system
is an optical microscope to aid in selection of the area to be analyzed.

An Acton(Cameca) electron probe microanalyser was used for this
study.

The metallographically polished specimens were placed in an
evaporator and coated with a carbon film of a few angstroms thickness
in order to provide electrical conductivity. Analyses were carried out under
the conditions of an accelerating voltage of 20 KV, an effective dia-
meter of 2 to 3 μ, a probe current of 0.04 μA, and a take-off angle of
18°. Pure iron and pure manganese were used as standard samples for the
alloys, while manganese sulfide (MnS) and iron sulfide (FeS) were used
for sulfur, iron and manganese in non-stoichiometric sulfides.

4.3.2 Calibration of Raw Intensity

Castaing[33] has derived an equation relating the relative inten-
sity of X-rays from alloys and pure elements. The weight fraction in the
first approximation is simply

$$\frac{I_{AB}}{I_{(A)}} = C_A \qquad (4.1)$$

where, I_{AB} and $I_{(A)}$ are the intensities of characteristic X-ray from alloy and pure standard element. However, it is invariably necessary to correct this approximation. First, X-rays generated within the sample by the electron beam are absorbed in passing from within the sample to the spectrometer where their intensities are measured. Secondly, characteristic X-rays of one element in the sample will be excited by the secondary fluorescence X-rays of other components or by the continuous X-ray spectrum of the sample. Finally, the variation of electron back-scatter with atomic number should be considered when the atomic numbers of the elements in the sample are largely separated.

In this study corrections for mass absorption and atomic number were calculated.

Castaing[34] introduced an X-ray production function to describe the distribution of characteristic X-rays as a function of the penetration depth, and Philibert[35] has expressed the absorption correction,

$$C_A = \frac{I_{AB}}{I_{(A)}} \frac{F(\mathcal{X})_A}{F(\mathcal{X})_{AB}} \tag{4.2}$$

where $F(\mathcal{X})_A$, and $F(\mathcal{X})_{AB}$ are the X-ray intensity functions of pure standard element and alloy, respectively. Theisen[36] has derived the intensity function:

$$F(\mathcal{X}) = \frac{1 + h}{(1 + \frac{\mathcal{X}}{\sigma})\left[1 + h(1 + \frac{\mathcal{X}}{\sigma})\right]} \tag{4.3}$$

where

$$h = 1.72 \cdot 10^{-6} \cdot \sigma_E \cdot V^2 \cdot \frac{A}{Z^2} \qquad (4.4)$$

V: accelerating voltage

A: atomic weight

Z: atomic number

σ_E is the effective Lenard coefficient which depends upon accelerating voltage and excitation of the characteristic radiation, V_c, and is given by

$$\sigma_E = \frac{8.9 \times 10^5}{(V - V_c)^2} \qquad , \qquad (4.5)$$

$$\chi = \frac{\mu}{\rho} \csc \phi \qquad , \qquad (4.6)$$

$\frac{\mu}{\rho}$ = mass absorption coefficient

and

ϕ = X-ray take-off angle .

Thomas[37] has derived the variation of the effective current factor R with atomic number Z due to electron back scattering. The effective current factor R decreases with increasing mean atomic number for a given ratio of initial electron acceleration to the critical excitation potential of the primary analyzed radiation, V/V_c, and the variation of effective current with atomic number is to a great extent independent of V/V_c if this ratio varies only between 2 and 7.6. The correction for

mass absorption and atomic number according to Theisen are

$$
\frac{I_{AB}}{I_{(A)}} = k_A = \frac{R_{AB}}{R_{(A)}} \cdot C_A \cdot \frac{F(\chi)_{AB}}{F(\chi)_A}
$$

$$
= \frac{R_{AB}}{R_{(A)}} \cdot C_A \cdot \frac{(1 + h_{AB})\left[1 + h_A \left(1 + \frac{\chi_A}{\sigma_E}\right)\right]\left(1 + \frac{\chi_A}{\sigma_E}\right)}{(1 + h_A)\left[1 + h_{AB}\left(1 + \frac{\chi_{AB}}{\sigma_E}\right)\right]\left(1 + \frac{\chi_{AB}}{\sigma_E}\right)} \quad .(4.7)
$$

For the alloy sample, h, χ , Z are the averaged values obtained by summing for all elements the product of the weight fraction and the variable. For example,

$$
h_{alloy} = \sum_i h_i c_i \quad . \tag{4.8}
$$

Tabulated values in Theisen's book were applied to the X-ray data.

Calibration curves for iron, manganese and sulfur in the iron-manganese-sulfur ternary system calculated from (4.7) are shown in Fig. 11, 12, and 13, respectively.
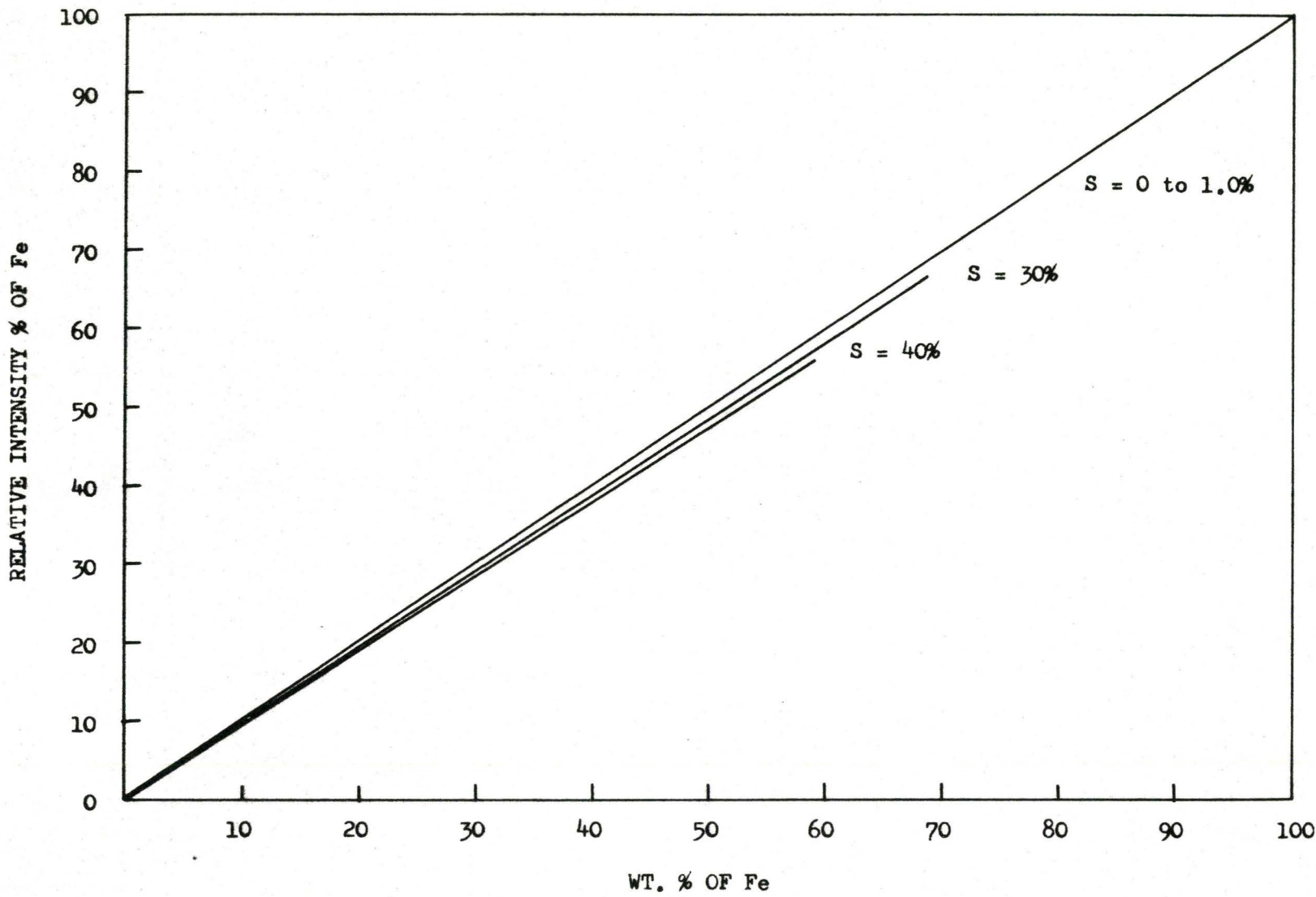
Fig. 11   Calibration curve for Fe in the Fe-Mn-S ternary alloys on $S_{K\alpha}$.
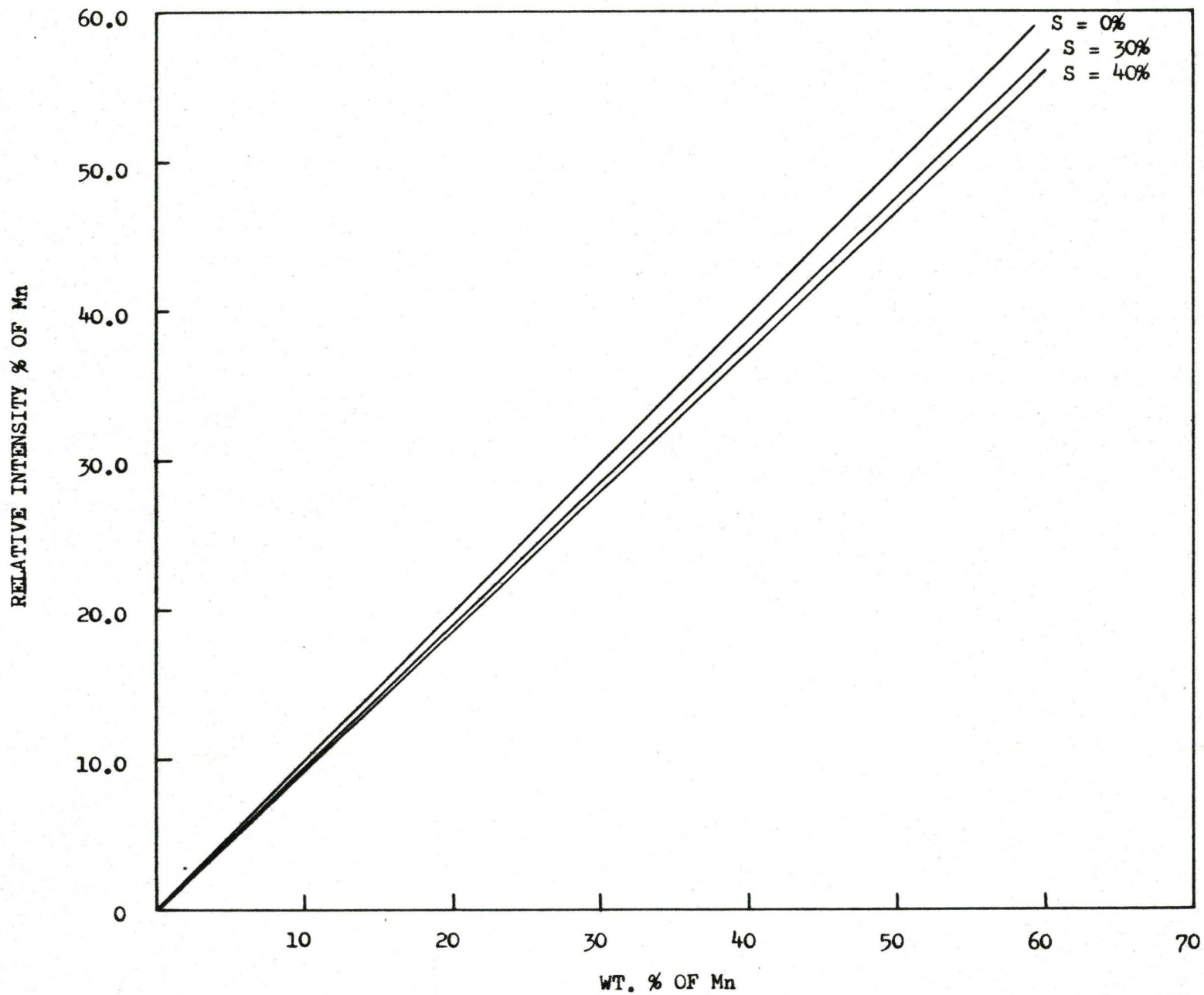
Fig. 12   Calibration curve for Mn in the Fe-Mn-S ternary alloys on $Fe_{K\alpha}$.
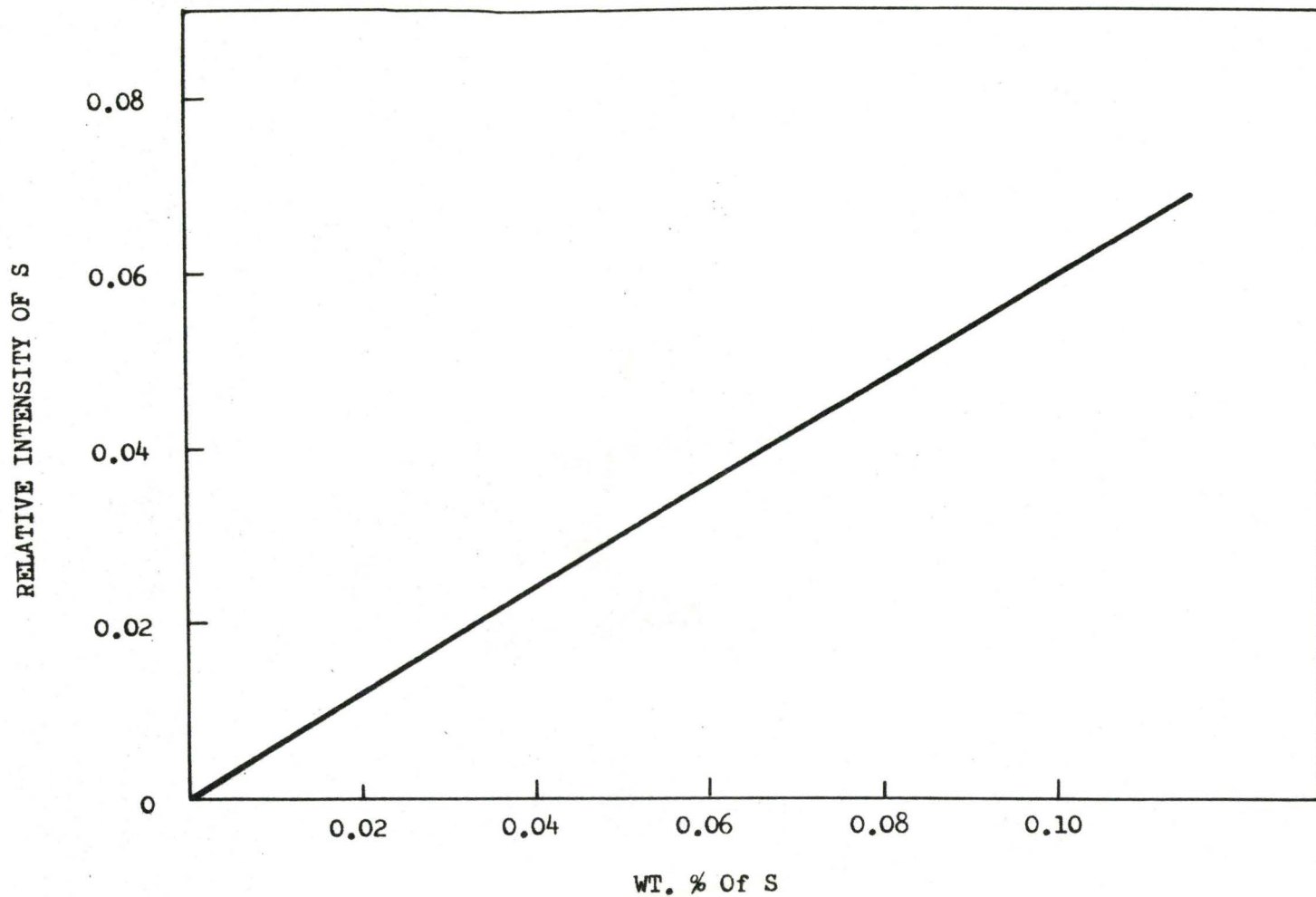
Fig. 13   Calibration curve for S in Fe rich corner of the Fe-Mn-S ternary alloys

on $S_{K\alpha}$.

CHAPTER V

EXPERIMENTAL RESULTS

The results for the manganese diffusion coefficient in γ-iron,
the three-phase equilibrium between γ-iron, FeS and MnS and the kinetic
experiments on the reaction of liquid FeS with MnS and Fe-Mn alloys with
MnS are presented in this section in the form of concentration-penetra-
tion curves, tables of electron probe microanalysis measurements and
photomicrographs. Experiments were carried out at 1300°C with the excep-
tion of manganese diffusion coefficient measurements which were carried
out at 1150°C, 1225°C, 1300°C and 1350°C.

5.1 Equilibrium between γ-Iron, FeS, and MnS at 1300°C

A three-phase equilibrated specimen of γ-Fe, liquid FeS, and
solid MnS was prepared in order to determine the solubilities of the
three components in each phase at 1300°C. Local equilibrium of the
three phases in the vicinity of a triple-point was assumed (see Fig. 14.)
Electron probe microanalysis of these locally equilibrated phases was
carried out on five different triple-points. Three to five points in
each phase close to the triple-point were measured. The intensities of
the X-rays and the corrected weight percentage are tabulated in Table
IV - 1 to 5. The solubilities of manganese and sulfur in γ-iron, and
manganese in liquid FeS were very low, while the solubility of iron in
solid MnS was found to be high. As can be seen from the tables, the

43
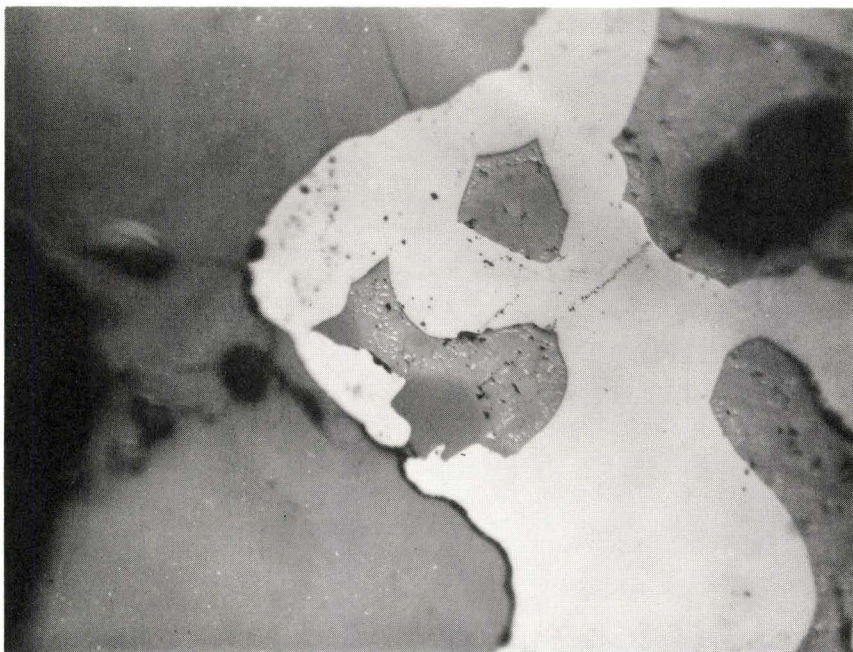
x 400
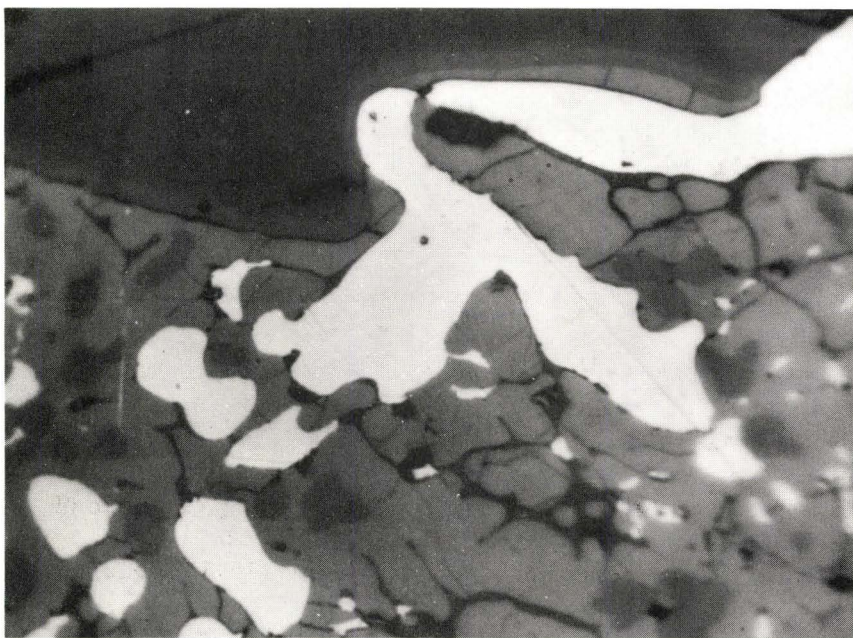
x 1600

Fig. 14   Photomicrographs of local equilibrium of the three phases,

Y-Fe, liquid FeS and MnS.

Table IV - 1

Microanalysis of Equilibrated
γ-Fe, liq. FeS, MnS Triple Points

Standard		Fe Intensity		Mn Intensity		S Intensity	
Initial	Fe	29411		280		434	
	Mn	144		146402		270	
	FeS	17345		259		33221	
	MnS	106		81772		34827	
Final	Fe	28872		347		407	
	Mn	135		144054		248	
	FeS	16266		235		30014	
	MnS	107		80175		33995	

Specimen		Fe		Mn		S	
γ-Fe		28402	96.86%	467	0.12%	470	0.030%
		28973	98.20	523	0.13	581	0.017
		28707	97.62	690	0.24	607	0.149
		29096	99.32	546	0.17	493	0.070
		29036	99.05	561	0.18	407	0
	Ave.		98.21		0.17		0.040
	wt.%		98.2±0.8		0.17±0.01		0.067±0.004
FeS		16503	62.36	3821	2.41	30810	35.52
		16845	63.67	2086	1.22	31912	36.77
		18702	70.63	1631	0.91	26711	30.73
		17710	66.70	1472	0.80	28217	32.49
		17053	64.45	1835	1.05	29554	34.53
	Ave.		65.56		1.29		34.01
	wt.%		65.6±0.6		1.34±0.03		34.0±0.5
MnS		6795	22.92	52511	40.86	33376	35.78
		6086	20.32	56977	44.35	33441	35.81
		7412	25.55	50054	38.95	32507	34.70
		6907	23.79	51557	40.13	32866	35.23
		6496	22.38	53072	41.30	33019	35.40
	Ave.		22.98		41.12		35.38
	wt.%		24.2±0.3		41.1±0.2		35.6±0.4

Table IV - 2

Microanalysis of Equilibrated
γ-Fe, liq. FeS, MnS Triple Points

Standard		Fe Intensity		Mn Intensity		S Intensity	
Initial Fe		29411		280		434	
	Mn	144		146402		270	
	FeS	17345		259		33221	
	MnS	106		81772		34827	
Final	Fe	28872		347		407	
	Mn	135		144054		248	
	FeS	16266		235		30014	
	MnS	107		80175		33995	

Specimen		Fe		Mn		S	
γ-Fe		28671	98.87%	404	0.06%	509	0.071%
		28491	98.23	605	0.20	445	0
		28356	97.76	578	0.18	578	0.130
	Ave.		98.29		0.15		0.067
	wt.%		98.3±0.8		0.15±0.01		0.101±0.004
FeS		17493	66.05	1084	0.75	31232	35.34
		18286	68.60	1221	0.63	30587	34.54
		17573	66.36	1226	0.63	31044	34.78
	Ave.		67.00		0.67		34.89
	wt.%		67.0±0.6		0.71±0.02		34.9±0.5
MnS		10724	36.20	33287	25.82	34371	36.82
		11448	38.72	29746	23.05	34477	36.91
		11603	39.62	26994	20.93	33710	36.10
		10514	35.92	31873	24.71	33929	36.33
	Ave.		37.62		23.63		36.54
	wt.%		39.4±0.3		23.6±0.2		36.8±0.4

Table IV - 3

Microanalysis of Equilibrated
Y-Fe, liq. FeS, MnS Triple Points

Standard		Fe Intensity		Mn Intensity		S Intensity	
Initial	Fe	32927		157		127	
	Mn	29		226916		115	
	FeS	21355		133		25868	
	MnS	30		127940		29079	
Final	Fe	31465		162		120	
	Mn	47		214514		139	
	FeS	20433		150		24143	
	MnS	28		120947		27484	

Specimen		Fe		Mn		S	
Y-Fe		32355	98.55%	564	0.18%	171	0.047%
		32318	98.75	445	0.13	165	0.036
		32364	99.11	527	0.16	169	0.047
		32101	98.60	476	0.14	223	0.102
		32050	98.67	303	0.08	172	0.051
	Ave.		98.74		0.14		0.057
	wt.%		98.7 ± 0.8		0.14 ± 0.01		0.094 ± 0.007
FeS		19408	59.00	1571	0.64	24981	36.45
		20470	62.23	1155	0.45	22368	32.64
		19877	60.43	1943	0.81	23774	34.84
		18891	57.42	2136	0.90	23825	34.77
		19532	59.37	1430	0.58	24936	36.39
	Ave.		59.69		0.68		35.02
	wt.%		59.7 ± 0.6		0.72 ± 0.03		35.0 ± 0.5
MnS		6644	20.75	81942	41.55	26714	35.82
		6475	20.27	84347	42.85	26978	36.17
		7017	21.99	76590	38.83	26752	35.88
		6739	21.17	78129	39.61	27871	37.01
		7053	22.24	73272	37.15	26914	36.09
	Ave.		21.28		40.00		36.19
	wt.%		22.4 ± 0.3		40.0 ± 0.2		36.4 ± 0.5

Table IV - 4

Microanalysis of Equilibrated
Y-Fe, liq. FeS, MnS Triple Points

Standard		Fe Intensity	Mn Intensity	S Intensity
Initial	Fe	28872	347	371
	Mn	121	144568	398
	FeS	16879	243	40905
	MnS	116	80816	43342
Final	Fe	26902	261	446
	Mn	147	143455	341
	FeS	16267	234	35471
	MnS	104	80121	41304

Specimen		Fe		Mn		S	
Y-Fe		27312	98.82%	456	0.14%	502	0.067%
		26694	96.55	560	0.19	425	0.011
		27039	97.82	445	0.11	497	0.060
		27067	98.18	534	0.18	531	0.088
		26984	98.09	572	0.21	492	0.056
	Ave.		97.89		0.17		0.056
	wt.%		97.9±0.8		0.17±0.01		0.091±0.004
FeS		16083	61.59	1076	0.56	37614	35.93
		16722	64.09	1050	0.54	36220	34.75
		17231	66.06	1312	0.72	35281	33.80
		15763	60.24	783	0.35	37811	36.10
		15854	60.81	1191	0.64	37355	35.72
	Ave.		62.56		0.56		35.26
	wt.%		62.6±0.6		0.60±0.03		35.3±0.4
MnS		8174	29.72	39925	31.18	41928	36.49
		8378	30.46	39453	30.82	41830	36.43
		8182	29.63	40016	31.26	40122	34.93
		7924	28.78	40434	31.59	41737	35.94
		8152	29.63	39796	31.09	39971	34.82
	Ave.		29.65		31.19		35.72
	wt.%		30.7±0.3		31.2±0.2		36.0±0.3

Table IV - 5

Microanalysis of Equilibrated
Υ-Fe, liq. FeS, MnS Triple Points

Standard		Fe Intensity		Mn Intensity		S Intensity	
Initial Fe		35172		148		114	
	Mn	45		247344		115	
	FeS	21064		132		26302	
	MnS	19		139357		29589	
Final Fe		32926		157		128	
	Mn	31		226919		117	
	FeS	20444		133		25370	
	MnS	30		25588		29083	

Specimen		Fe		Mn		S	
Υ-Fe		34466	98.33%	565	0.11%	190	0.061%
		34253	98.15	604	0.18	184	0.060
		34879	98.95	497	0.14	196	0.062
		34121	98.55	662	0.21	218	0.075
		34327	99.57	533	0.16	196	0.062
	Ave.		98.71		0.17		0.064
	wt.%		98.7 ± 0.8		0.17 ± 0.01		0.089 ± 0.007
FeS		20726	63.43	1570	0.59	25164	35.54
		20441	62.55	1427	0.53	25453	35.94
		20037	61.32	1691	0.65	25045	35.36
		20773	63.58	1534	0.58	24803	35.02
		19584	59.92	1257	0.47	25769	36.39
	Ave.		62.16		0.56		35.65
	wt.%		62.2 ± 0.6		0.59 ± 0.03		35.7 ± 0.5
MnS		10164	30.15	63533	29.98	27840	34.97
		11059	32.96	60014	28.31	25697	32.27
		10697	32.03	65358	30.84	26264	32.99
		10085	30.31	59936	28.27	28136	35.32
		9355	28.23	69354	32.71	27447	34.56
	Ave.		30.74		30.02		34.02
	wt.%		32.4 ± 0.3		30.0 ± 0.2		34.3 ± 0.5

scatter of the data for Fe in MnS between different triple points is rather

high. From experiments, described below it will accrue that the approach

to equilibrium is unpredictably slow in this three phase system, particularly

in the MnS phase. The other experiments indicate that the triple point analyzed

in Table IV - 2 is the only one which has attained a state close to equilibrium.

We therefore summarize our best normalized solubility values from this experi-

ment as follows:

Table V

The compositions of γ-Fe, Liquid-FeS, and Solid MnS

equilibrated for 60 min. at $1300^{\circ}C$

(in weight %)

	Fe	Mn	S
Fe	99.8 ± 0.8	0.15 ± 0.01	unreliable
Liquid FeS	63.5 ± 0.6	0.71 ± 0.03	35.8 ± 0.5
Solid MnS	39.4 ± 0.3	24.4 ± 0.2	36.2 ± 0.5

5.2 Measurement of Manganese Diffusion Coefficient in γ-Iron

The diffusion coefficient of manganese in γ-iron up to a manganese

content of 6.14% was measured at $1150^{\circ}C$, $1225^{\circ}C$, $1300^{\circ}C$ and $1350^{\circ}C$ using iron-

manganese infinite diffusion couples. A typical concentration-penetration curve

is shown in Fig. 15. The probability plot of concentration for this penetration

curve is shown in Fig. 16. It is clear that to a good approximation the

concentration-penetration curve fits to an error function so that manganese

diffusion coefficient in γ-iron up to 6.14% of manganese concentration is

independent of concentration. Therefore, the diffusion coefficient of manganese

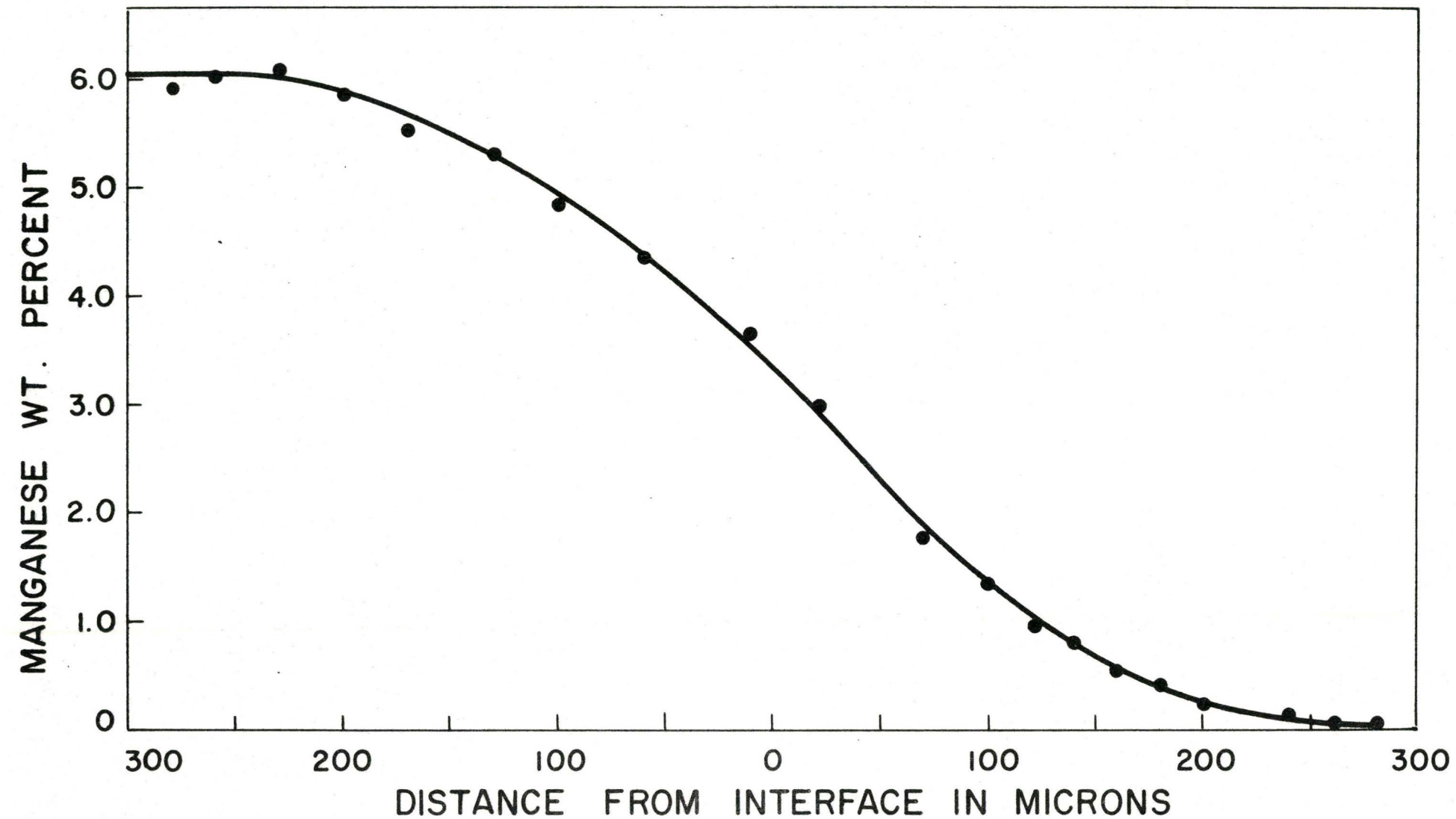in iron could be calculated from equation (3.10). This calculation yields
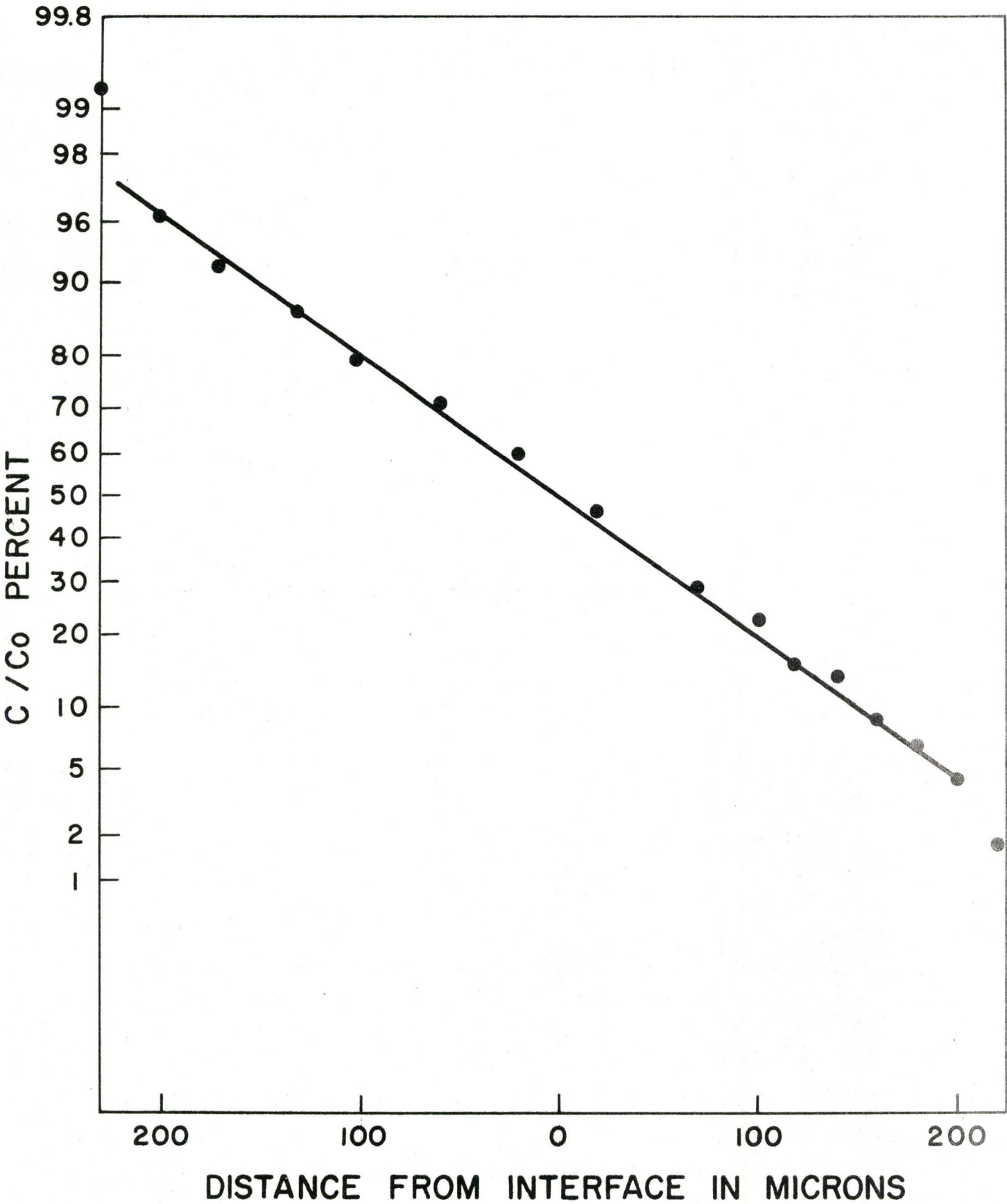
Fig. 15   Concentration-penetration curve of manganese in Fe-6.14% Mn vs. Fe diffusion couple

annealed for 13 hrs. at 1300°C.

$$D = \frac{z^2}{\pi t} = \frac{(128 \times 10^{-4})^2}{3.14 \times 13 \times 3600} = 1.12 \times 10^{-9} \quad cm^2/sec \ . \ (5.1)$$

The coefficients at 1150°C, 1225°C and 1350°C were similarly calculated. The complete results are tabulated in Table VI.

<div align="center">Table VI</div>

<div align="center">Diffusion Coefficient of Manganese in γ-Iron (0 - 6.14% Mn)</div>

Temperature °C	D_{Mn}
1150	$7.67 \times 10^{-11} \quad cm^2/sec$
1225	2.38×10^{-10}
1300	1.12×10^{-9}
1350	2.23×10^{-9}

5.3 Liquid FeS vs. Solid MnS Diffusion Couples

Diffusion couples between liquid FeS and solid MnS at 1300°C were prepared in order to investigate the existence of the pseudo-binary system of FeS-MnS, to determine the solubility of iron in manganese sulfide and to determine the diffusion rate of Fe in MnS.

Synthesized and sintered FeS was evacuated in a quartz tube together with solidified MnS. At 1300°C the FeS melted instantly and a liquid FeS vs. solid MnS diffusion couple was formed. The diffusion couples were annealed for 6, 30 and 60 min. at 1300°C. The concentration-penetration curves of these diffusion couples are shown in Fig. 17, 18 and 19, respectively. A micrograph of the 6 min. couple near the liquid-solid interface is shown in Fig. 20. From the probe traces and
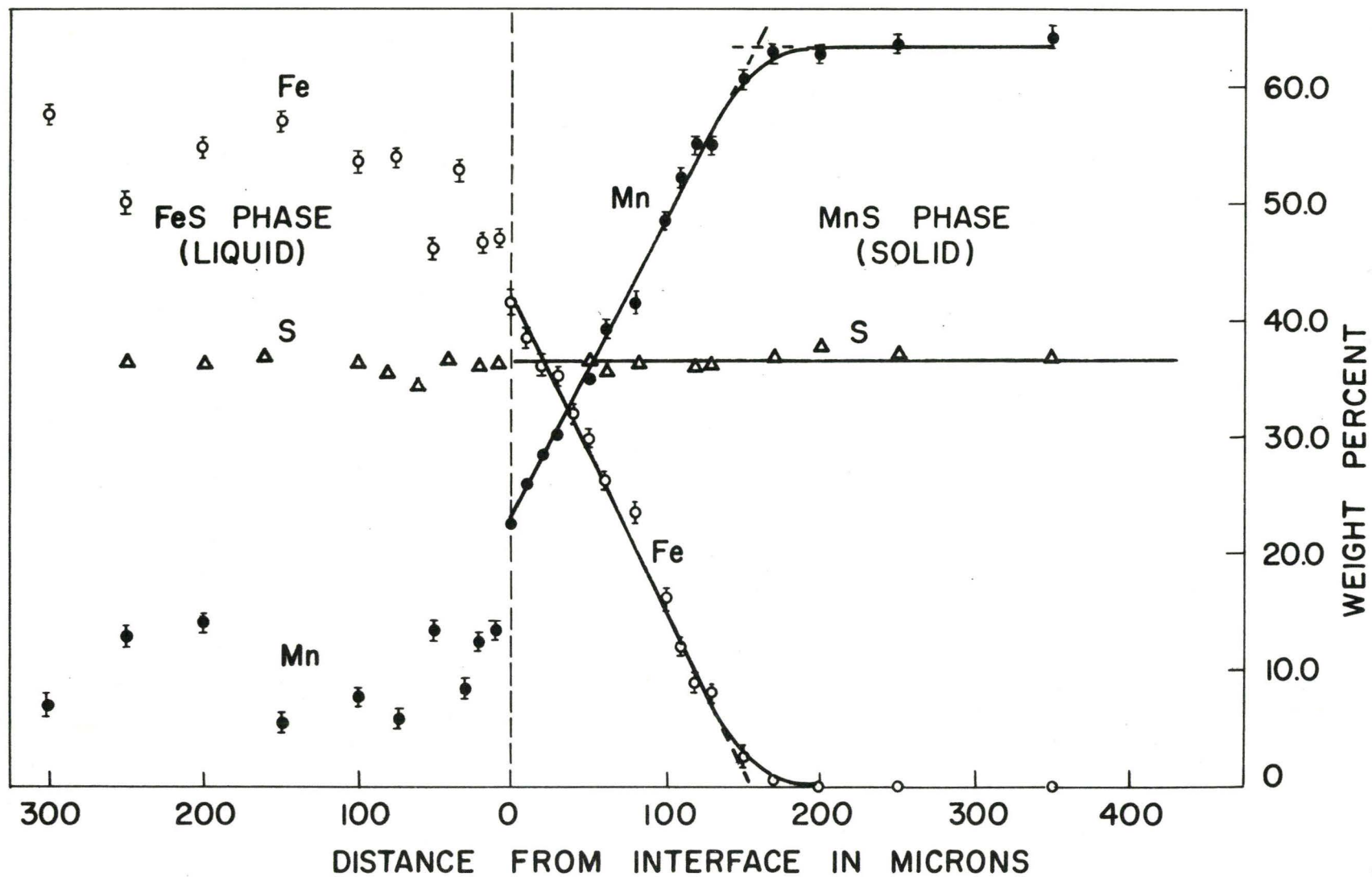
Fig. 17   Concentration-penetration curve for the FeS-MnS couple diffused for 6 min.
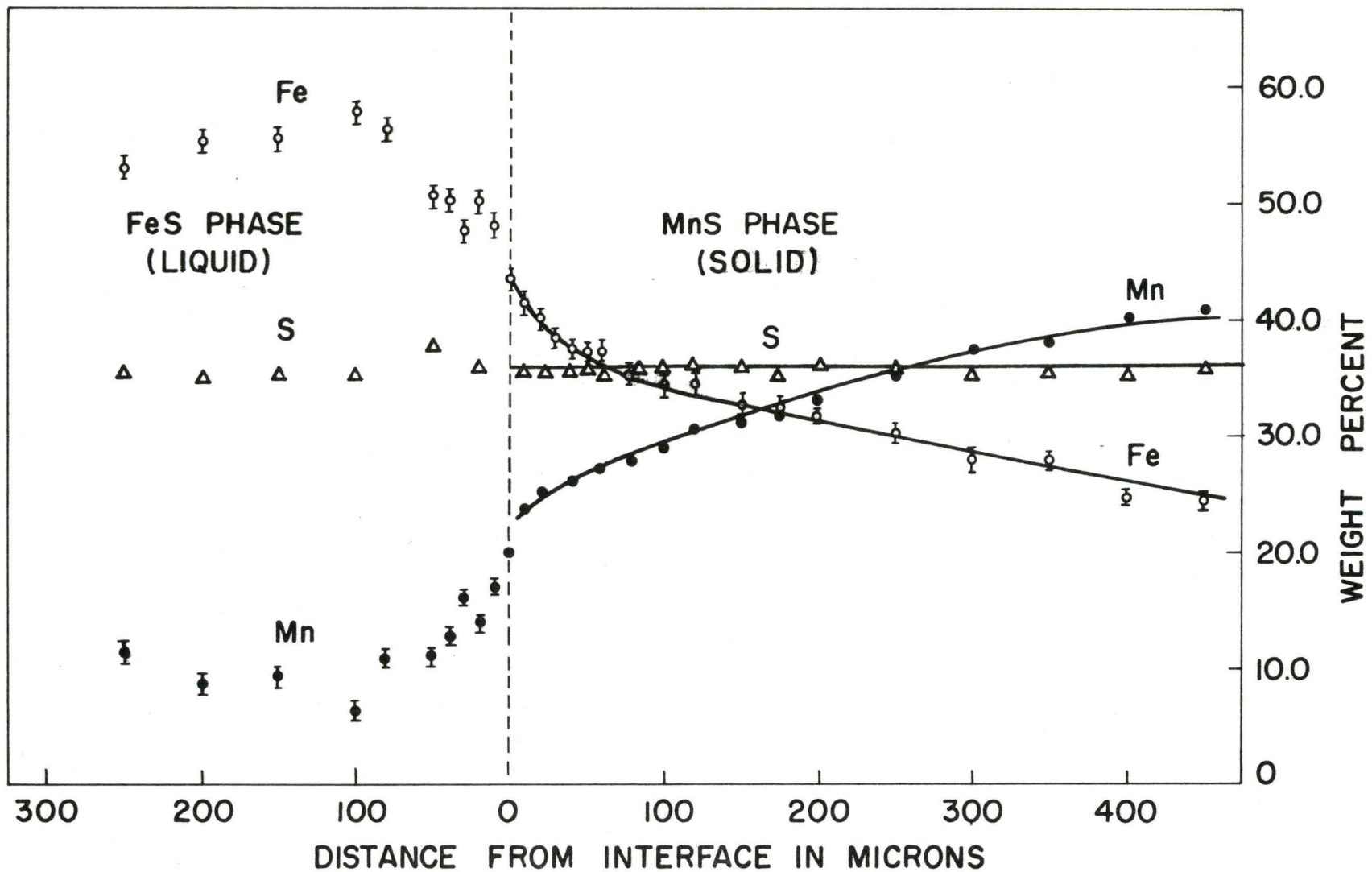
Fig. 18 Concentration-penetration curve for the FeS-MnS couple diffused for 30 min.
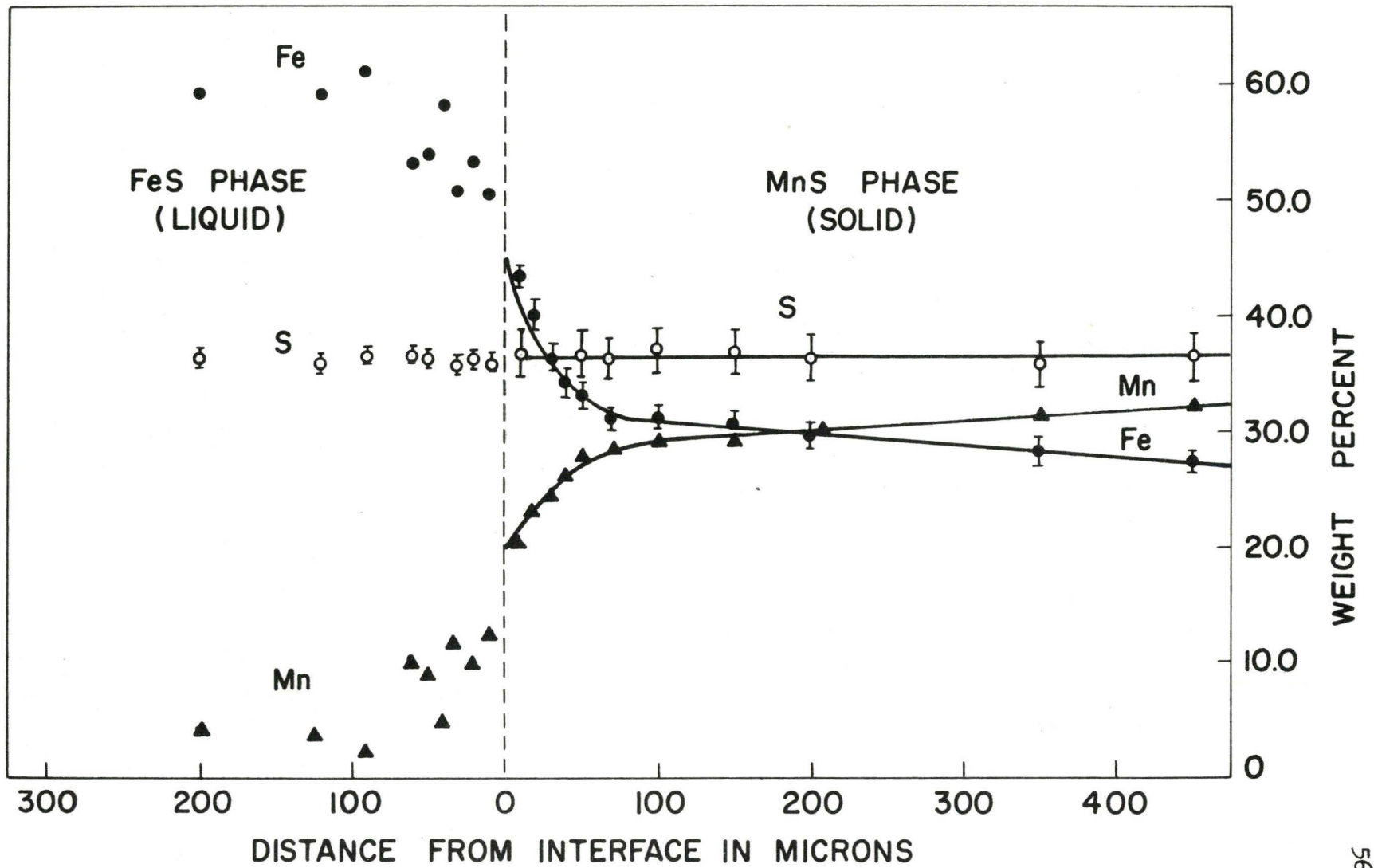
Fig. 19   Concentration-penetration curve for the FeS-MnS diffusion couple diffused for 60 min.

Fig. 20   Photomicrograph of the liquid-solid interface of the FeS-MnS

diffusion couple annealed for 6 min.   x 1600

micrographs it was observed that the iron penetrated into the solid MnS phase from the liquid phase as an anomolous function of time, while the manganese rapidly penetrated into the liquid FeS from the solid MnS phase. At the same time FeS penetrates dendritically to a considerable depth to form a two-phase mixture of solid manganese sulfide and liquid iron sulfide. This two-phase mixture is apparent in the FeS side of the penetration curve of Fig. 17.

5.4 Iron-Manganese Alloy vs. MnS Diffusion Couples

The kinetics of reaction between iron-manganese alloys and MnS at 1300°C was investigated by the infinite diffusion couple method.

The penetration curves for pure iron vs. MnS couples diffused for 8 and 35.33 hrs. are shown in Fig. 21 and 22, respectively. A micrograph of the planar interface after 8 hrs. is shown in Fig. 23.

Although the original interface of these couples was not perfectly straight, it was none the less assumed for quantitative analysis that approximately unidirectional diffusion took place across the interface.

The penetration curves for the Fe-1.08% Mn vs. MnS couple diffused for 6 hrs. and for the Fe-9.30% Mn vs. MnS couple diffused for 7.5 hrs. are shown in Fig. 24 and 25, respectively. A micrograph of the inter-face of the Fe-1.08% Mn vs. MnS is shown in Fig. 26. It is to be noted that despite precautions, oxygen-rich phases appeared sporadically along the interface. These regions were always avoided for purpose of micro-probe analysis.

The depletion of manganese in the matrix and the formation of fine precipitates of manganese sulfide in the alloy phase near the
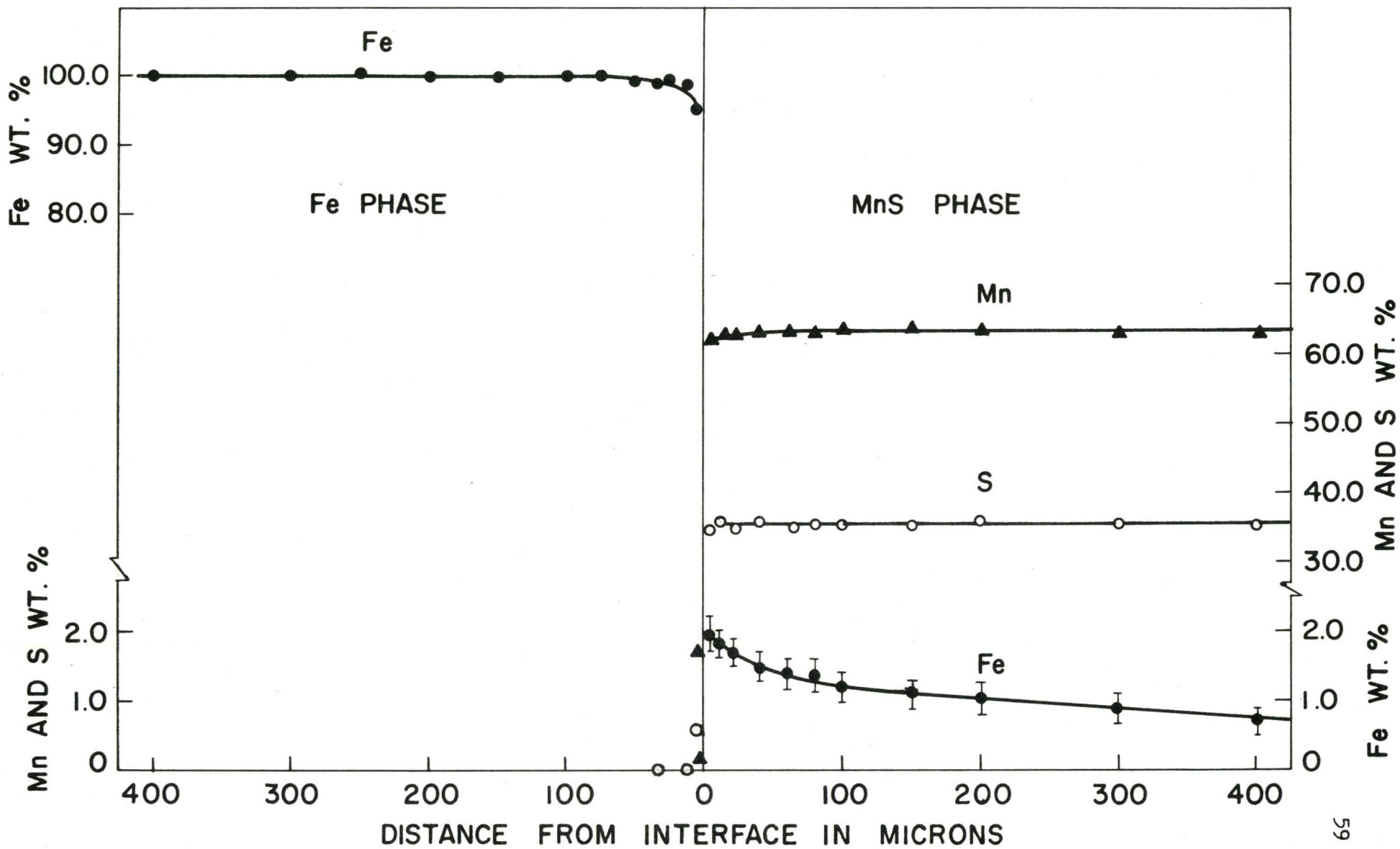
Fig. 21   Concentration-penetration curve for the Fe vs. MnS couple diffused for 8 hrs.

Fig. 22   Concentration-penetration curve for the Fe vs. MnS couple diffused for 35.33 hrs.

Fig. 23   Photomicrograph of the planar interface of the Fe vs. MnS

couple diffused for 8 hrs.   x 400

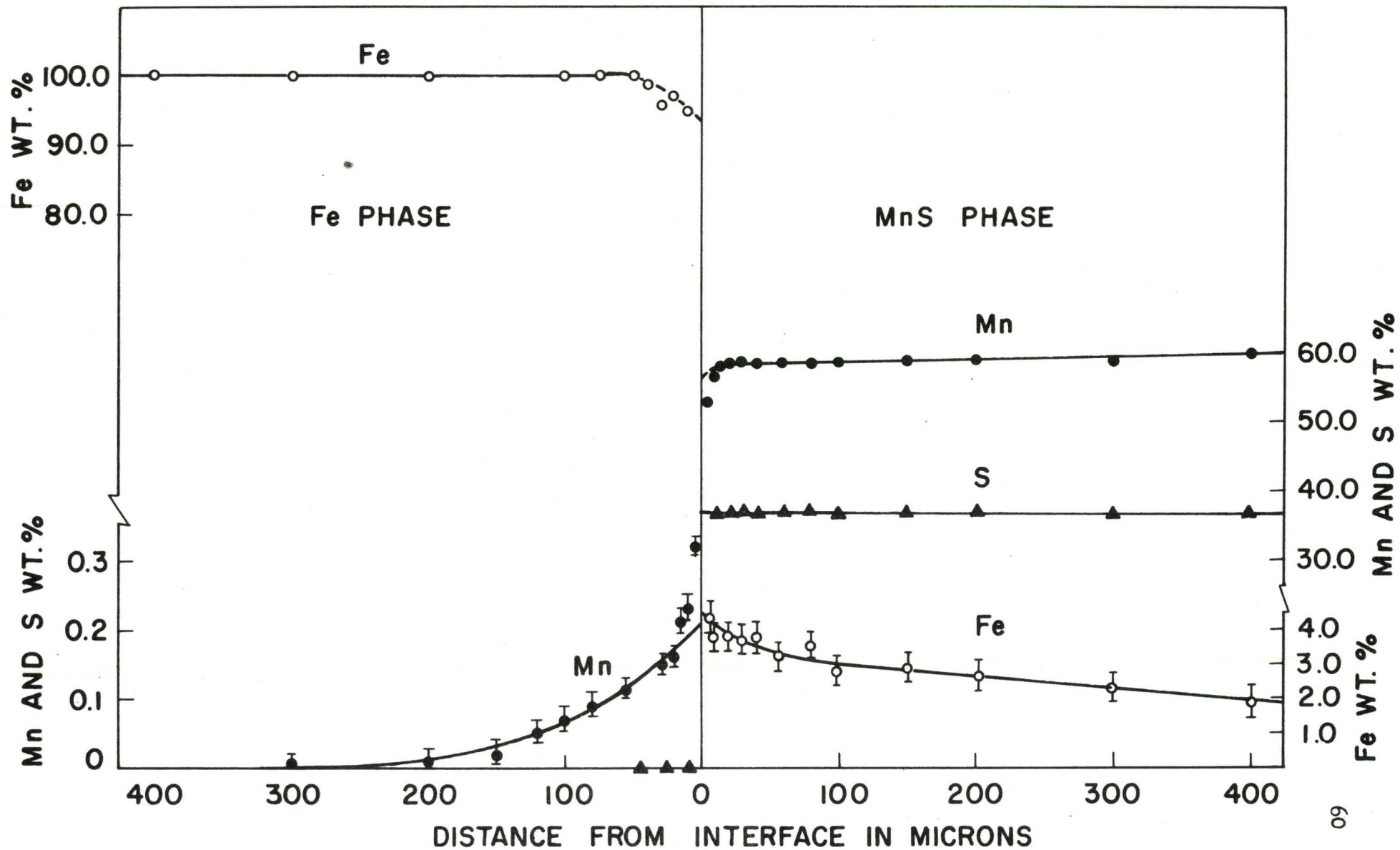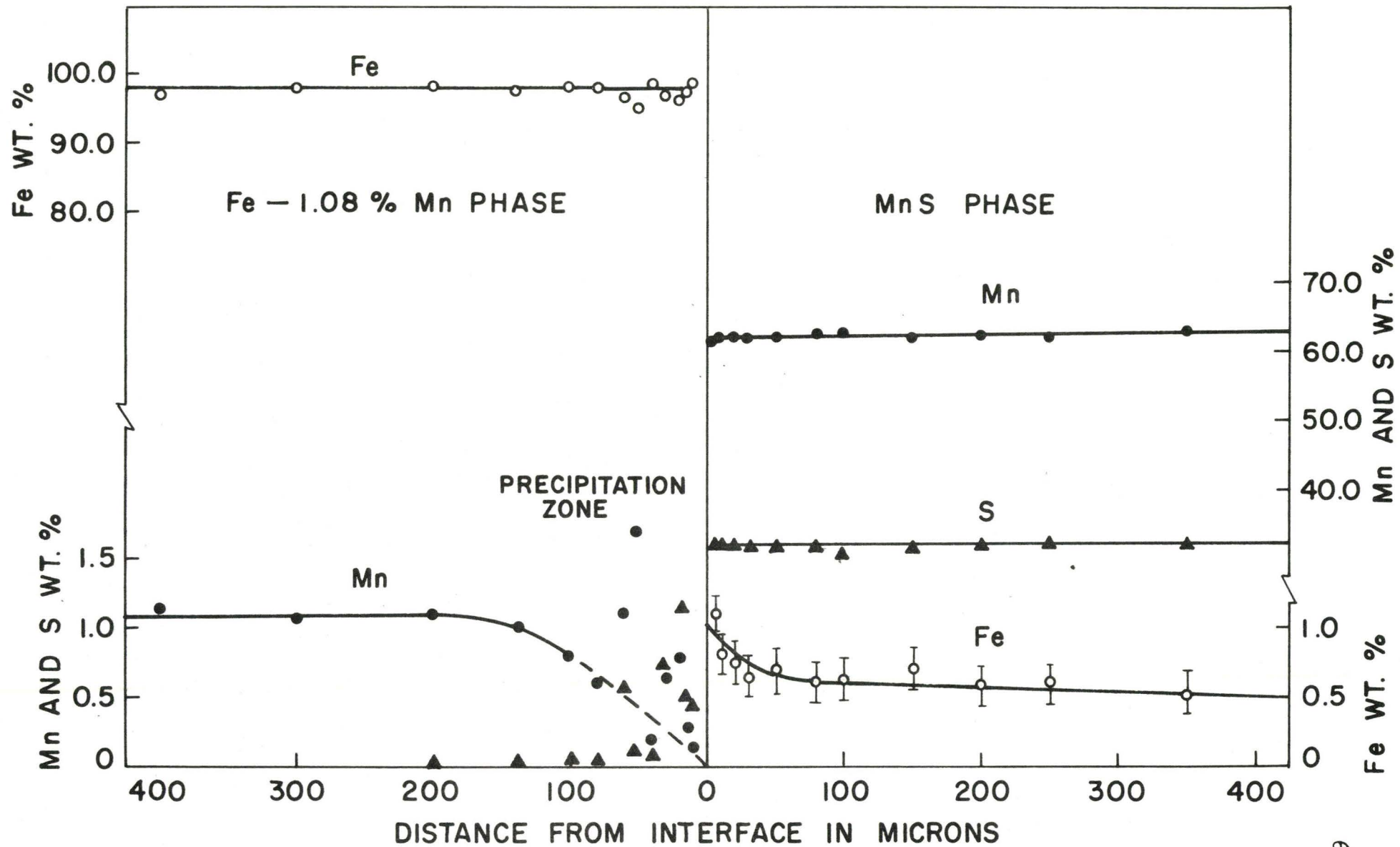Fig. 24   Concentration-penetration curve for the Fe-1.08% Mn vs. MnS couple diffused for 6 hrs.
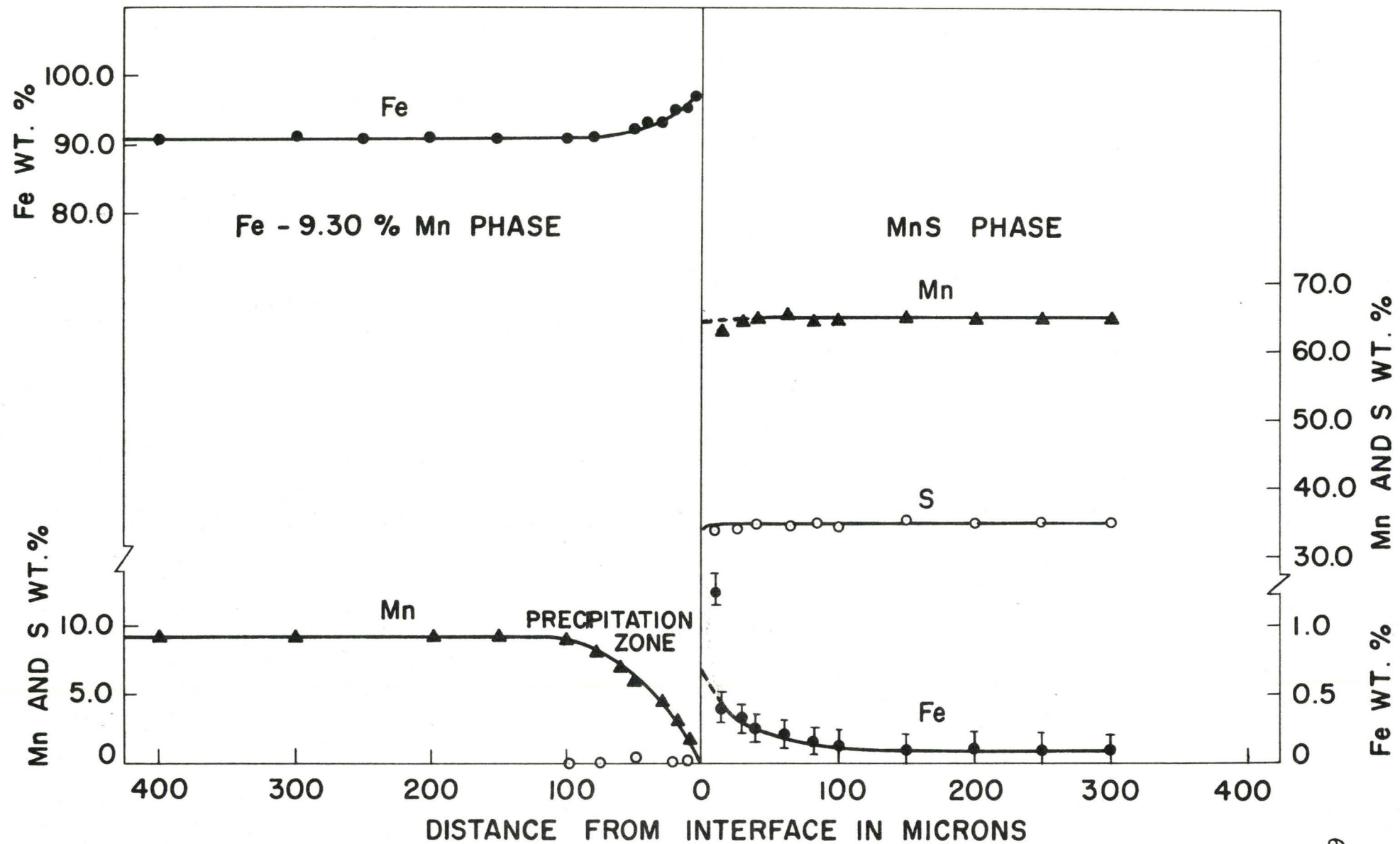
Fig. 25   Concentration-penetration curve for the Fe-9.3% Mn vs. MnS couple diffused for 7.5 hrs.
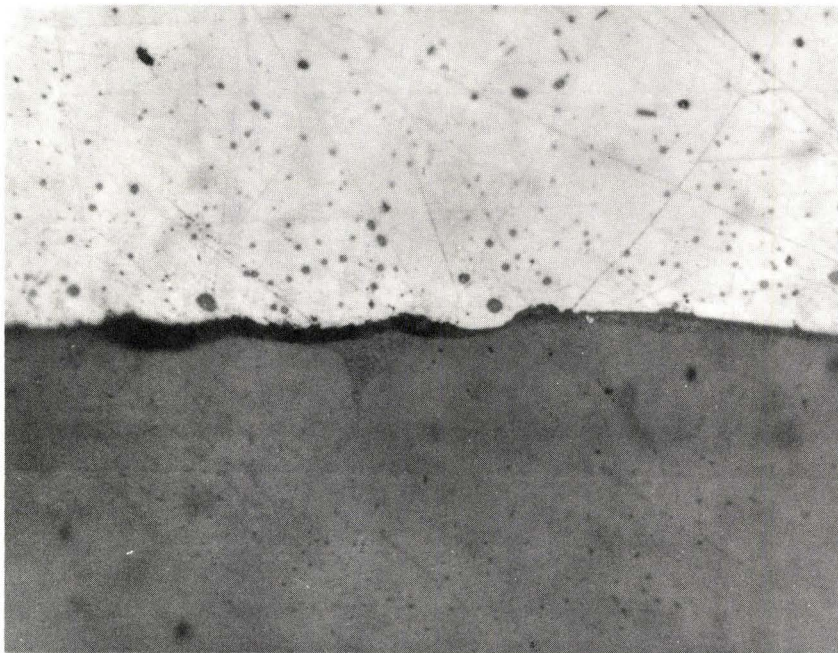
Fig. 26   Photomicrograph of the interface of the Fe-1.08% Mn vs. MnS
couple diffused for 6 hrs. x 400

interface were observed. The time dependence of the growth of this precipitated zone was investigated for reaction between an Fe-4.52% Mn alloy and MnS annealed for various times between 4 to 25 hrs. The width of the zone was equated with the manganese depleted zone determined by microprobe analysis (cf. Fig. 25). The results are tabulated in Table VII.

Table VII

Manganese Depleted Zone Width as a

Function of Time

Mn Composition	Time (hrs.)	Distance (μ)
	4.0	78 ± 10
	9.0	129 ± 12
4.52 %	16.0	175 ± 14
	25.0	201 ± 16

CHAPTER VI

DISCUSSION

The experimental results will be discussed mainly from the point-of-view of the kinetics of sulfide transformations. The single equilibrium experiment on the equilibrium of γ-iron, liquid FeS and MnS provides the boundary conditions for the kinetic discussion.

6.1 Equilibrium of γ-Iron, FeS and MnS

The equilibrium experiment was undertaken in order to resolve some doubts left by the three-phase equilibrium data of Clark[3]. This experiment was carried out using very high purity iron and oxygen free sulfides whose compositions were close to stoichiometric. The present design and preparation of specimens was such as to provide a coarse phase structure and was therefore more amenable to accurate microprobe analysis.

Considering the low concentration level, the results shown in Table IV - 1 to 5 show a fair consistency of the values of manganese and sulfur concentrations in the γ-iron phase equilibrated with liquid FeS and MnS and of the manganese concentration in the liquid FeS equilibrated with γ-iron and MnS. However, the measured iron concentrations in MnS equilibrated with γ-iron and liquid FeS, which should be much more accurate, show a considerable variation. Since the measurements were made within 10 microns of the boundaries one might attribute the

variation to accidentally oblique emergence of the measured phase. However, the experiments discussed in sections 6.3 and 6.4 suggest that the measurements are correct and that all but one of the triple points had not obtained true equilibrium. We therefore place reliance on this single experiment (Table IV-2).

Since error due to oblique emergence and near approach of the probe spot to the interface is possible, particularly at low concentration levels, we are forced to state that in Table V, the values of 0.15% and 0.71% for manganese in Y-iron and liquid FeS may be on the slightly high side and that the sulfur values given in Table IV (~0.08%) are completely unreliable. This latter is brought sharply into focus by the fact that Turkdogan[12] gives a sulfur solubility in Fe-0.15% Mn of ~0.009%. It is noted that Clark was unable to record measurements in this low concentration range.

We therefore summarize the results of our equilibrium experiment for the three-phase Y-Fe, FeS, MnS triangle at $1300^{\circ}C$ in table V subject to the reservations stated above. Below we describe a kinetic experiment which removes the uncertainty concerning the solubility of iron in MnS.

6.2 The Manganese Diffusion Coefficient in Y-Iron

Fig. 27 shows the data from Table VI in the form of an Arrhenius plot. For comparison is shown the results of Wells and Mehl[14] calculated from their expression for 4% Mn and 0.02% C

$$D = (0.57 \pm 0.11) \exp \left(- \frac{66200 \pm 500}{RT} \right) \quad . \tag{6.1}$$

Our values are consistent with their activation energy but are about twice as great as this within our narrow range of experiments.
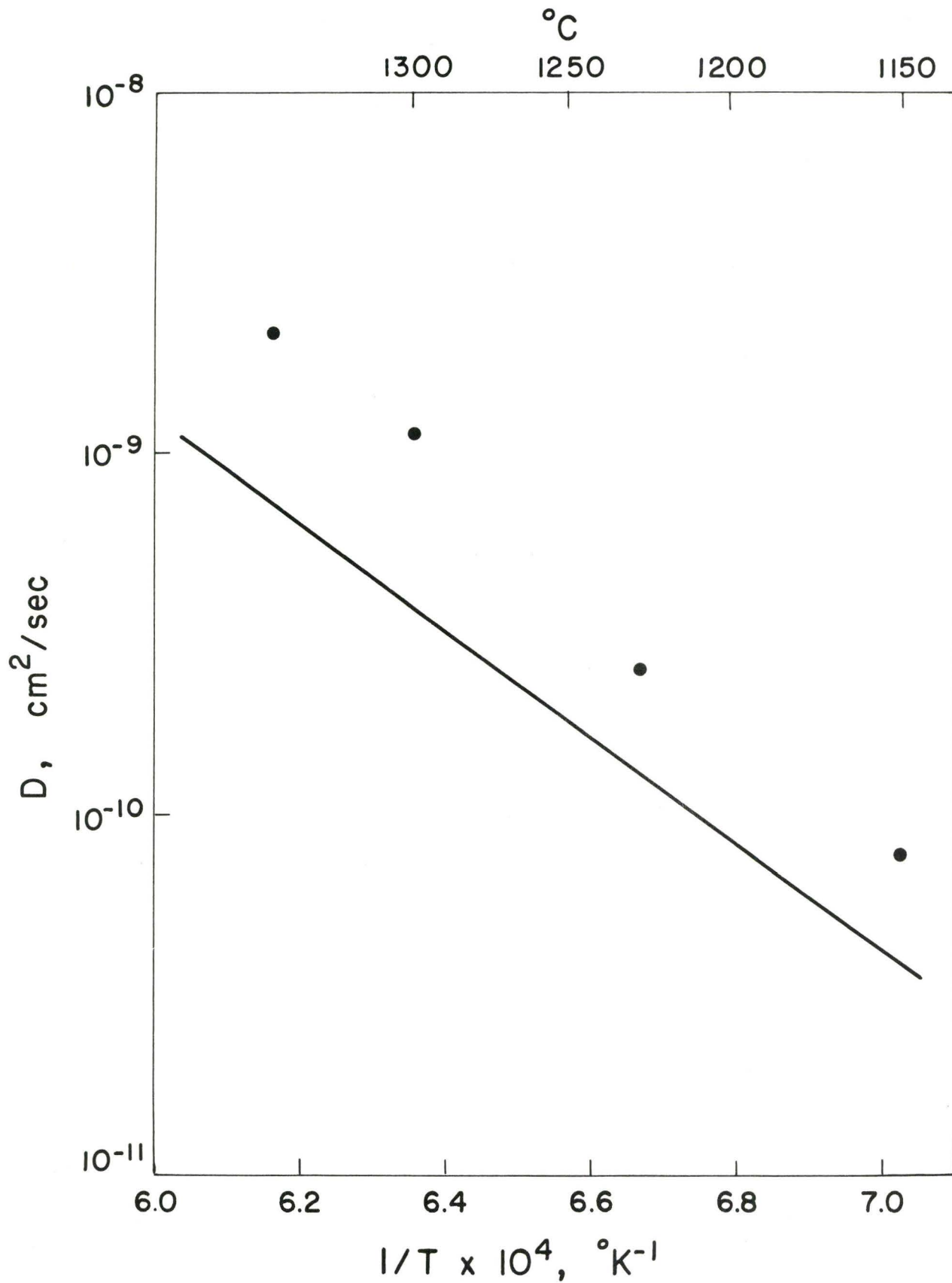
Fig. 27   Temperature dependence of the diffusion coefficient of

manganese in γ-iron. Solid line after Wells and Mehl[14].

At the moment we have no explanation for the discrepancy. In the diffusion calculations presented below our own value for $1300^{o}C$ was used.

6.3 Liquid FeS vs. Solid MnS Diffusion Couple

Diffusion couples between stoichiometric liquid FeS and solid MnS were prepared and examined so as to determine the equilibrium between the two phases, to determine the kinetics of the resulting reaction and to check the proposition that a pseudo-binary eutectic system is formed along the constant sulfur surface. The diffusion penetration curves of Figs. 17, 18 and 19 show that the iron exchanges with the manganese in MnS as an anomolous function of time although in every case the concentration of iron extrapolates to approximately 41.0 wt.% at the interface of the FeS rich phase. We regard this as our best value for the solubility of iron in MnS equilibrated with liquid FeS. This is to be compared with an average value of 30.2% obtained in the equilibrium experiments. Note, however, that one of the experiments (Table IV - 2) gives a value of 39.4%. We conclude that the corresponding triple point is the only one which has approached close to equilibrium and therefore yields reliable solubility data for the other phases.

It is to be noted from the micrograph of Fig. 20 and the microprobe traces that the FeS side of the couple has become a two-phase mixture of MnS and FeS during the course of reaction. It is particularly significant that no iron phase appears anywhere within the sample. This is very good evidence that a pseudo-binary does in fact exist and that Clark's observation to the contrary is incorrect.

The course of the reaction can be understood from an observation of the probe traces (Figs. 17, 18 and 19) and the micrograph. In the

early stages manganese diffuses rapidly through the liquid FeS as iron counter-diffuses into the MnS. The manganese rapidly reaches the saturation level ($\leq$0.71% Mn) in the liquid and since the solid diffusion gradient must continue to deliver manganese to the liquid phase, the saturation limit will then be exceeded and MnS will start to precipitate. This probably occurs by dendritic projection from the existing solid MnS interface. We assume that the end-point of the reaction would occur when the iron profile in a finite sample of MnS reaches uniformity. The sample could then be an equlibrium mixture of FeS and MnS.

The diffusion coefficient of iron or manganese in MnS can be determined from Fig. 17 using equation (3.10), assuming concentration independence. This gives

$$D_{Fe}, D_{Mn} \text{ (in MnS)} = \frac{Z^2}{\pi t} = \frac{(150 \times 10^{-4})^2}{3.14 \times 6 \times 60}$$
$$= 2.0 \times 10^{-7} \quad cm^2/sec \quad . \tag{6.2}$$

The diffusion rate in the MnS phase is therefore much greater than that in the γ-iron phase. This can be understood on the premise that MnS is a metal deficit semiconductor and has a high density of lattice defects which aid the diffusion process.

Note, however, that the penetration as a function of time is not parabolic. Indeed, the penetration following anneals of 30 min and 6 min is much greater than would be predicted from the above value of D. This unusual characteristic may be associated with the peculiar defect structure of MnS described below.

6.4 Iron-Manganese vs. MnS Diffusion Couples

Further important kinetic information was obtained from a series of iron-manganese alloy vs. MnS diffusion couples.

As seen in Fig. 23 the interface of the pure iron sample remained stable throughout the reaction. Note also that the time dependence of the reaction (cf. Figs. 21 and 22) is non-parabolic and therefore cannot be simply described by a diffusion model with constant interface compositions determined by the phase diagram. Indeed, during the first 8 hrs. negligible manganese has diffused into the iron, corresponding to a zero interface concentration. Iron, on the other hand, has diffused deeply into the MnS and has attained an interfacial concentration of $\sim$ 2% Fe. After 35.33 hrs., manganese has begun to diffuse into the iron (the diffusion length is consistent with our measured D_{Mn} = 1.1 x 10^{-9} cm^2/sec) and has attained an interface composition of $\sim$ 0.2% while the iron interface concentration in the MnS has risen to $\sim$ 4% and penetrated further into that phase. Further evidence of the change in interface concentration is to be found in the shape of the penetration curves which are much steeper at the interface than would be the case with a constant driving potential (cf. Figs. 21 and 22).

In examining the mass balance we find that, while considerable iron has diffused into the MnS, practically no manganese diffused out. It can only be concluded that deviations from the stoichiometry of MnS must be taking place to accomodate the mass balance.

The alloy couples (see Figs. 24, 25 and 26) are similar in character with the exception that internal sulfidation of the manganese in the iron has in every case occurred. The "sub-precipitate" depth for the 4.52% Mn couple appears to follow a parabolic law (Fig. 28). We may understand the occurrence of the "sub-precipitates" by calculating the "virtual" path in the iron phase using the empirical interface concentration ($\sim$ 0.2% Mn) and Turkdogan et al.[12]'s phase diagram.
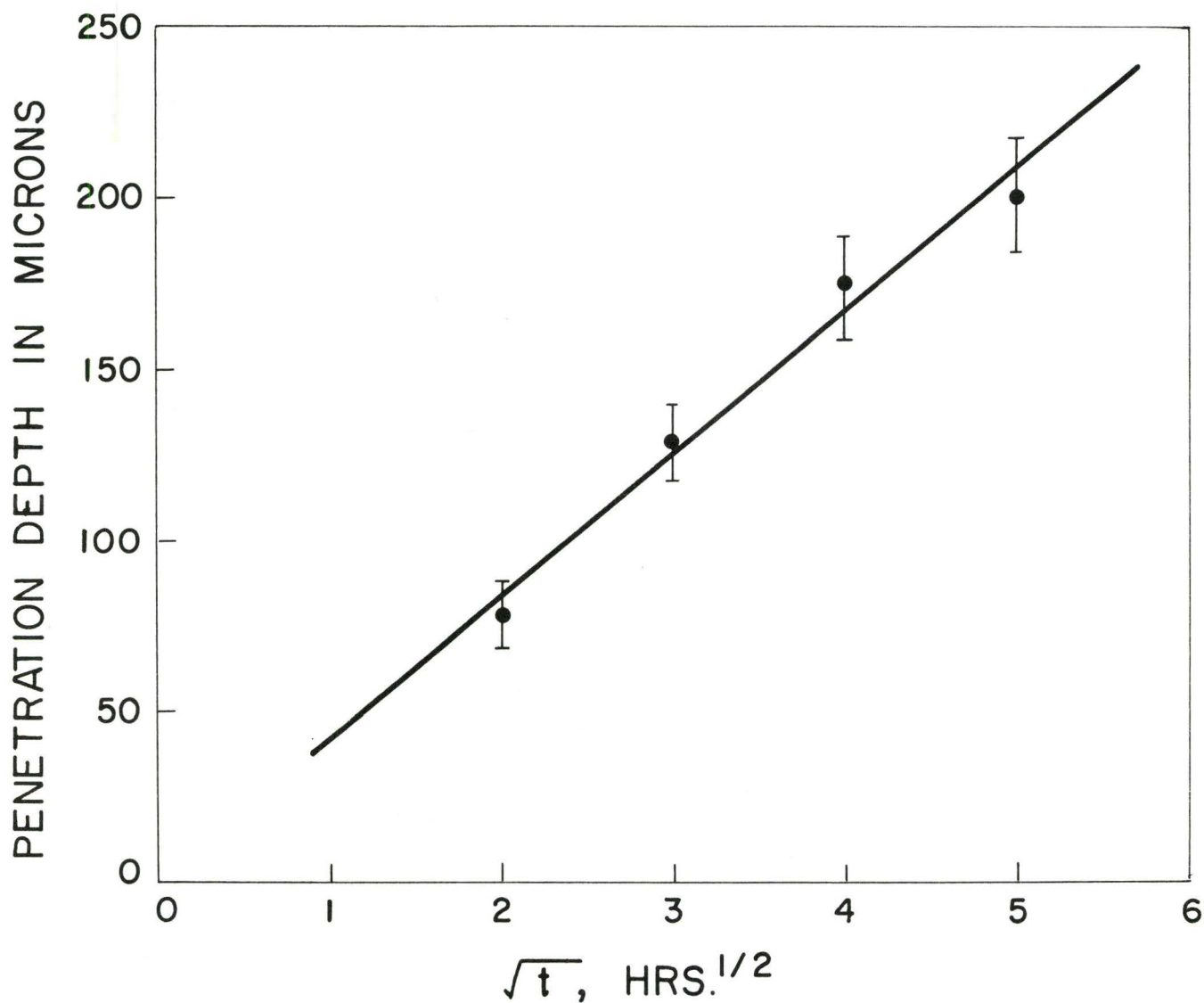
Fig. 28   Parabolic growth of penetration depth of MnS precipitates

in Fe-Mn alloy phase for Fe-4.52% Mn vs. MnS diffusion

couples.

The calculated virtual path[*] using $D_{11} = 7.9 \times 10^{-9}$ cm^2/sec and $D_{22} = 1.1 \times 10^{-9}$ cm^2/sec is shown in Fig. 29 and this clearly indicates a high supersaturation level which must lead to precipitation. From Fig. 28 we note that the empirical rate law for the precipitation depth in the 4.52% Mn couple is

$$\xi = 6.9 \times 10^{-5} \, t^{\frac{1}{2}} \quad \text{cm/sec}^{\frac{1}{2}} \quad . \tag{6.3}$$

This is to be compared with the sulfur diffusion length,

$$\xi' = \sqrt{D_{11} \, t} = 28 \times 10^{-5} \, t^{\frac{1}{2}} \quad \text{cm/sec}^{\frac{1}{2}} \quad . \tag{6.4}$$

Since MnS precipitation is occurring it is to be expected that the sulfur penetration depth will be foreshortened, and a factor of four less than for free diffusion does not appear unreasonable.

Although it had been our original hope to obtain further information about the phase diagram (particularly the two phase tie-lines between Fe-Mn and MnS) and about the diffusion kinetics of reaction of Fe-Mn and MnS, the anomalous reaction behaviour mitigates against a simple analysis for the required data. We must therefore be content at

---

[*] Using Turkdogan's value $\varepsilon_{12} = -9.06$ and equations (3.18) and (3.19) we find that D_{12} and D_{21} are several orders of magnitude smaller than the on-diagonal coefficients so the cross-terms in the diffusion equations may be neglected.
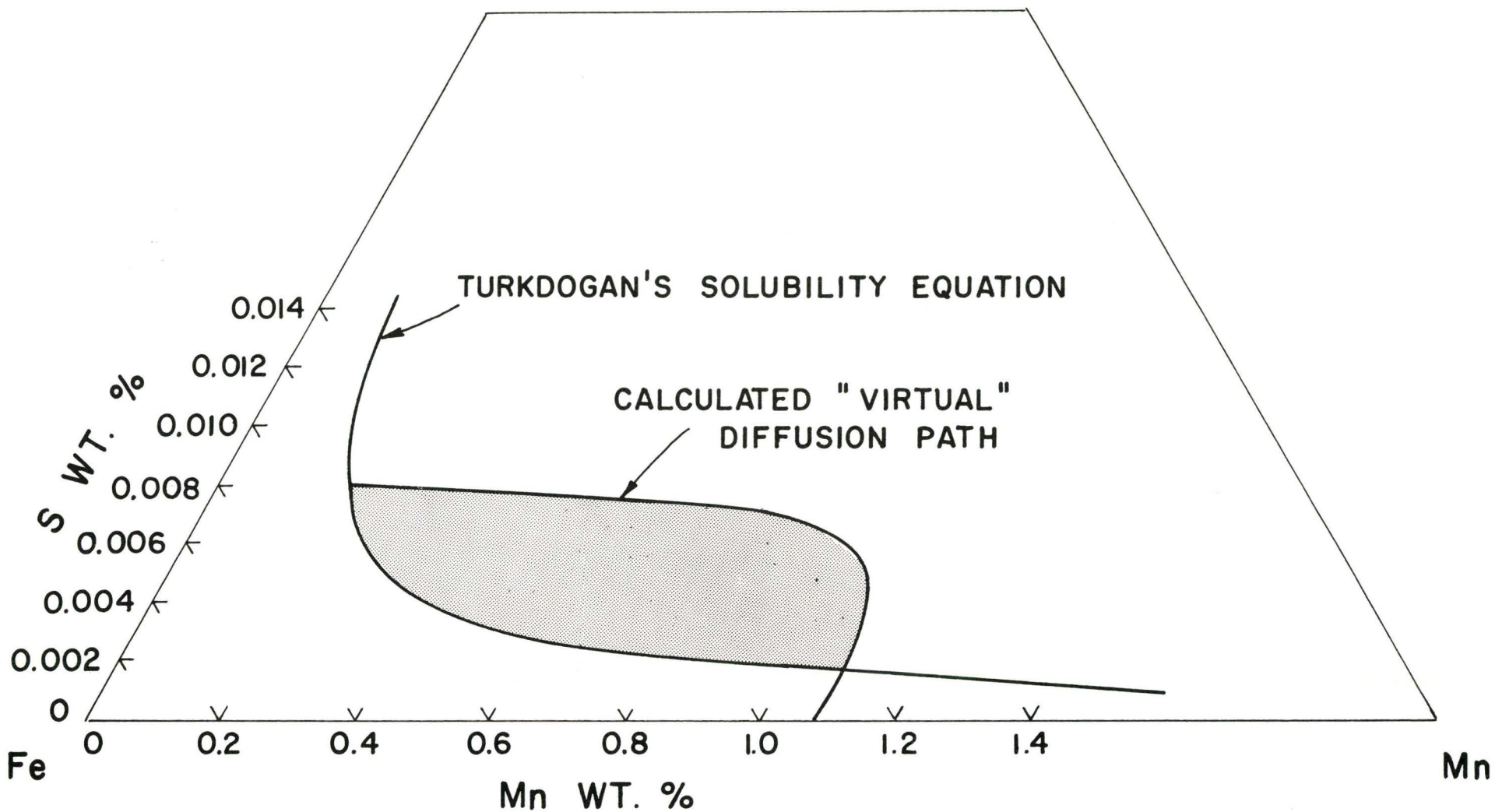
Fig. 29   Calculated "virtual" diffusion path using $D_{11} = 7.9 \times 10^{-9}$ cm^2/sec and $D_{22} = 1.1 \times 10^{-9}$ cm^2/sec, which indicates a high supersaturation level within the γ-phase.

this time with qualitative inferences from the observations.

The results require that the MnS phase contains a significant composition range (~2% from stoichiometry). Since MnS is thought to be a metal deficit semiconductor it could very easily accomodate a variation of the metal to sulfur ratio through filling of vacant sites. This characteristic could also explain the anomalous diffusion behaviour evidenced in Figs. 17, 18 and 19. If the vacant sites tended to be saturated near the interface but not at depth then we would expect a much greater rate of penetration at depth than near the interface.

The semiconductive electrical character of the MnS might also be invoked to explain the anomalous kinetics of the metal-sulfide reaction. It is well-known that large electrical potential differences (~1 volt) exist at metal-semiconductor interfaces[38]. This potential difference could act as a diffusion barrier and give the impression of chemical reaction control.

6.5 An Experimental Test of the Diffusion Formalism and the Data

To test the technological significance of our material we have undertaken the prediction of the outcome of a simple experiment. This is designed to simulate the course of the reaction which would take place between a liquid FeS precipitate and an alloy matrix as a sample of steel is cooled from the melting temperature or is soaked at a fixed high temperature, e.g. 1300°C. Our starting point is, of course, the premise that the initial sulfide which forms from the steel melt is iron rich[2] [3].

A sample of Fe-6.14% Mn alloy was placed in an evacuated quartz tube covered by roughly an equal amount of powdered stoichiometric FeS and was rapidly heated to a reaction temperature of 1300°C. It was held at the temperature for 40 minutes and then quenched in ice water.

We therefore have a diffusion couple between liquid FeS and
the alloy. The "virtual" path calculated on the basis of our data is
shown in Fig. 30 in relation to our measured phase diagram. In prepar-
ing this diagram we have assumed that a very rapid solution reaction
for the alloy in the liquid occurs at the beginning. The upper section
of the "virtual" path therefore describes the evolution of the liquid
composition as it moves towards the composition of the γ-FeS phase
boundary during the solution reaction. The attainment of this state
defines the initial condition for our theoretical discussion. That is,
at time zero, we have FeS of composition 0.54% Mn and 31.5% S in local
equilibrium with the alloy phase interfacial composition of 0.114% Mn
and 0.018% S. Since only a small amount of sulfur goes into the metal
during the subsequent reaction we may assume that the interface does
not move substantially. Therefore, the diffusion paths in the metal will
be those corresponding to a simple semi-infinite diffusion couple.

We note that the "virtual" path for the metal passed through
four phase regions, i. e., L + γ, γ + L + MnS, γ + MnS and γ. We may
therefore expect instabilities to develop in the two phase regions.
(Three-phase regions on diffusion paths within infinite couples appear
only as the contact point between two 2-phase regions and are therefore
of infinitely small extent[24]). Fig. 31, which is a micrograph of this
couple clearly shows these instabilities as they have developed during
the reaction. We note first the unstable interface between FeS and
γ-Fe due to the supersaturation of the γ-phase with respect to sulfur.
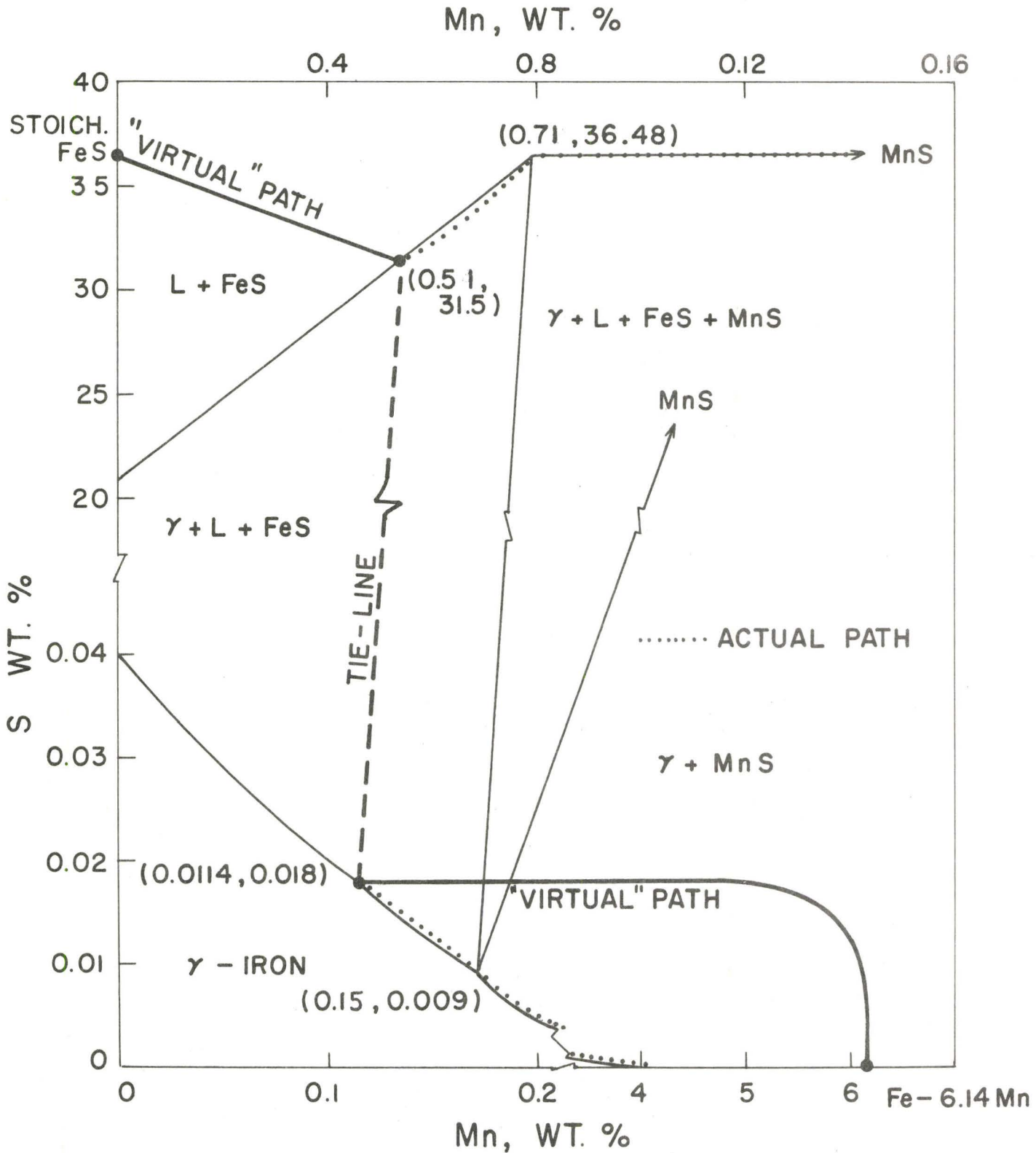We note also the MnS precipitates which have appeared within the metal

Fig. 30   Calculated "virtual" diffusion path between Fe-6.14% Mn
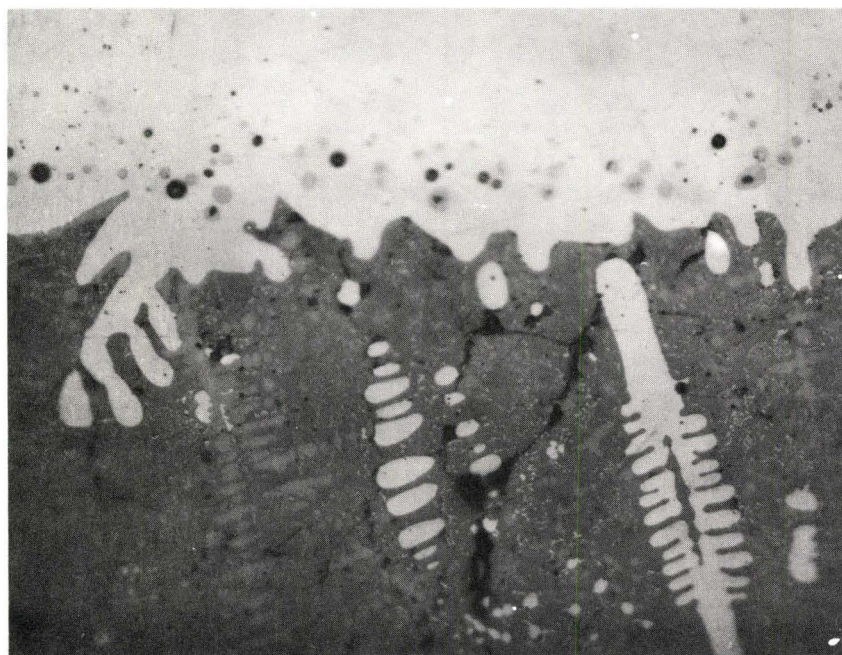
and liquid FeS.

Fig. 31   Photomicrograph of the interface of the Fe-6.14% Mn vs.
liquid FeS diffusion couple diffused for 40 min. x 400

in an isolated array. This behaviour is very similar to that observed
in the earlier experiments, and indeed, the "virtual" path for this region
is also very similar (cf. Fig. 29).

We imagine that the precipitation reactions move the "virtual"
diffusion path towards the phase boundary to produce the real paths
indicated by the dotted lines. We may expect that there is a small remaining
supersaturation which is needed to continuously drive the precipitation,
and in the case of the γ-FeS reaction, we may expect that the super-
saturation will be distributed to both ends of the tie-line. Hence,
γ will tend to grow into the liquid in co-operation with liquid growing
into the γ. The γ-dendrites which appear in the micrograph may be
explained in this way.

The late progress of the reaction is rather complicated because
the sulfide phase is finite in extent rather than infinite. Since Mn
continues throughout the reaction to diffuse into the liquid we may
expect the liquid composition to ultimately reach the upper corner
of the three-phase triangle and then move to the right towards the MnS
phase. Thus a fairly uniform three-phase region is expected to form in the
formerly liquid zone with the amount of MnS increasing with time at the
expense of the FeS. There should be no change in the amount of γ-iron
during this stage of the reaction since the path must move along the
top of the three-phase region.

A number of the characteristics of sulfides in commercial steels
are explained by this analysis and experiment. Firstly, if the manganese
content is too low it may not be possible to deliver sufficient manga-
nese from the metal to convert the FeS to MnS so the embrittling phase

remains in the finally cooled ingot, leading to hot shortness in sub-sequent hot-working operations. Secondly, the solid surrounding sul-fides will be strongly depleted in manganese as has been often observed by microprobe analysis[1]. Thirdly, iron intrusions are often observed in the sulfides in steel and these are undoubtedly due to the same unstable conditions which led to the iron dendrites in the sulfide phase of our large experimental sample. Finally, very fine angular precipi-tates of MnS are often observed in steels and cast irons along with the more common course lenticular type. These could derive from the inter-nal sulfidation reaction predicted and observed in the present investiga-tion.

CHAPTER VII

SUMMARY

1. A number of important elements of the phase equilibrium in Fe-Mn-S at 1300°C have been recorded. These are summarized, along with the data of other investigators in Fig. 32. We wish to emphasize that our stated manganese solubilities in FeS and γ-iron may be on the high side.

2. The diffusion coefficient of Mn in γ-iron was determined in the temperature range 1150°C to 1350°C. The values are about twice as great as those reported by Wells and Mehl[14].

3. The diffusion coefficient of Fe or Mn in MnS is at least 2.0×10^{-7} cm^2/sec at 1300°C, the value increasingly sharply upwards with deviations from stoichiometry.

4. The reaction between Fe-Mn alloys and MnS cannot be understood on the basis of simple diffusion theory. We suppose that this is due to the semi-conductive character of MnS which in contact with iron may produce an electrical potential barrier which inhibits diffusion across the interface.

5. MnS has a finite solubility range (~2%) which is probably due to its supposed metal deficit structure.

6. The constitutional and diffusion data has successfully predicted the character of the reaction between liquid FeS and Fe-6.14% Mn.
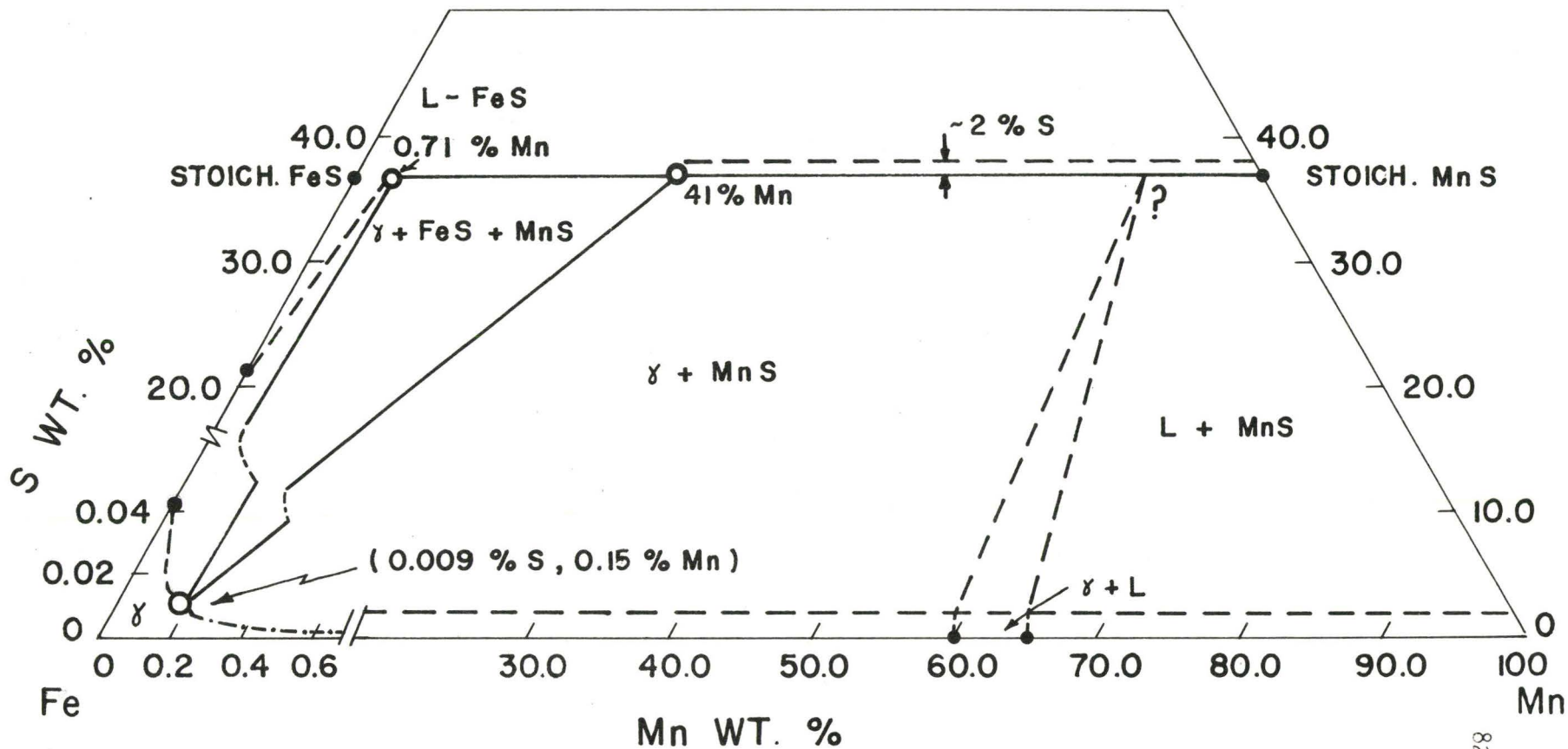
Fig. 32 Summary of the constitution diagram of the Fe-Mn-S system at 1300°C.

REFERENCES

1. Kirkaldy, J. S., Brigham, R. J., Domian, H. A. and Ward, R. G., Can. Met. Quart., 2, 233, (1963).

2. Kirkaldy, J. S., Progress Report No. 13 to AISI, June, 1966.

3. Clark, I. S. R., Master's Thesis, McMaster Univ., 1965.

4. Wentrup, H., Techn. Mitteilung Krupp, 5, 131, (1937).

5. Hansen, M., Constitution of Binary Alloys, McGraw-Hill, New York, 1958.

6. Vogel, R. and Hotop, W., Arch. Eisenhuttenw., 11, 41, (1937 1938).

7. Schnaase, H., Z. Physik. Chem., B 20, 89, (1933).

8. Kroger, F. A., Z. Krist., 100, 543, (1939).

9. Jensen, E., Am. J. Sci., 240, 695, (1942).

10. Chao, H. C., Van Vlack, L. H., Oberin, F. and Thomassen, L., Trans. ASM, 57, 885, (1964).

11. Rosenqvist, T. and Dunicz, B. L., Trans. AIME, 194, 604, (1952).

12. Turkdogan, E. T., Ignatowicz, S. and Pearson, J., JISI, 180, 349, (1955).

13. Brown, J. R., JISI, 205, 154, (1967).

14. Wells, C. and Mehl, R. F., Trans. AIME, 145, 315, (1941).

15. Bramley, A., Haywood, F. W., Cooper, A. T. and Watts, J. T., Trans. Farad. Soc., 31, 707, (1935).

16. Ainslie, N. G. and Seybolt, A. U., JISI, 194, 341, (1960).

17. Kononyuk, I. F., Phys. Met. Metallog., 19, 159, (1965).

18. Onsager, L., Ann. N. Y. Acad. Sci, $\underline{46}$, 241, (1945).

19. Barrer, R. M., Diffusion in and through Solids, Cambridge University Press, 1951.

20. Fujita, H. and Gosting, L. J., J. Am. Chem. Soc., $\underline{78}$, 1099, (1956).

21. Kirkaldy, J. S. and Purdy, G. R., Can. J. Phys., $\underline{40}$, 208, (1962).

22. Darken, L. S., Trans. AIME, $\underline{180}$, 430, (1949).

23. Rhines, F. N., Meussner, R. A., DeHoff, R. T., Trans. AIME, $\underline{212}$, 860, (1958).

24. Kirkaldy, J. S. and Brown, L. C., Can. Met. Quart. $\underline{2}$, 89, (1963).

25. Meijering, J. L., Discussion to reference 26.

26. Clark, J. B. and Rhines, F. N., Trans. ASM, $\underline{51}$, 199, (1959).

27. Kirkaldy, J. S. and Fedak, D. G., Trans. AIME, $\underline{224}$, 490, (1962).

28. Kiessling, R. and Westman, C., JISI, $\underline{204}$, 377, (1966).

29. Furuseth, S. and Kjekshus, A., Acta Chemica Scandinavica, $\underline{19}$, 1405, (1965).

30. Argyriades, D., Derge, G. and Pound, G. M., Trans. AIME, $\underline{215}$, 909, (1959).

31. ASTM X-Ray Data File No. 6-0518.

32. Meites, L. and Meites, T., Anal. Chem. $\underline{20}$, 984, (1948).

33. Castaing, R., X-Ray Optics and X-Ray Microanalysis, Academic Press, New York, 1963.

34. Castaing, R., Thesis, Univ. of Paris, 1951.

35. Philibert, J., X-Ray Optics and X-Ray Microanalysis, Academic Press, New York, 1963.

36. Theisen, R., Quantitative Electron Microprobe Analysis, Springer-Verlag New York, New York, 1965.

37. Thomas, P. M., Brit. J. Appl. Phys. $\underline{14}$, 397, (1963).

38. Kittel, C., Introduction to Solid State Physics, p. 388, John Wiley & Sons, New York, 1956.